

AD-A066 649

SOUTHWEST RESEARCH INST SAN ANTONIO TEX

F/6 11/4

DAMAGE MECHANISMS AND FAILURE OF 3-D CARBON-CARBON COMPOSITES. (U)

N00014-77-C-0510

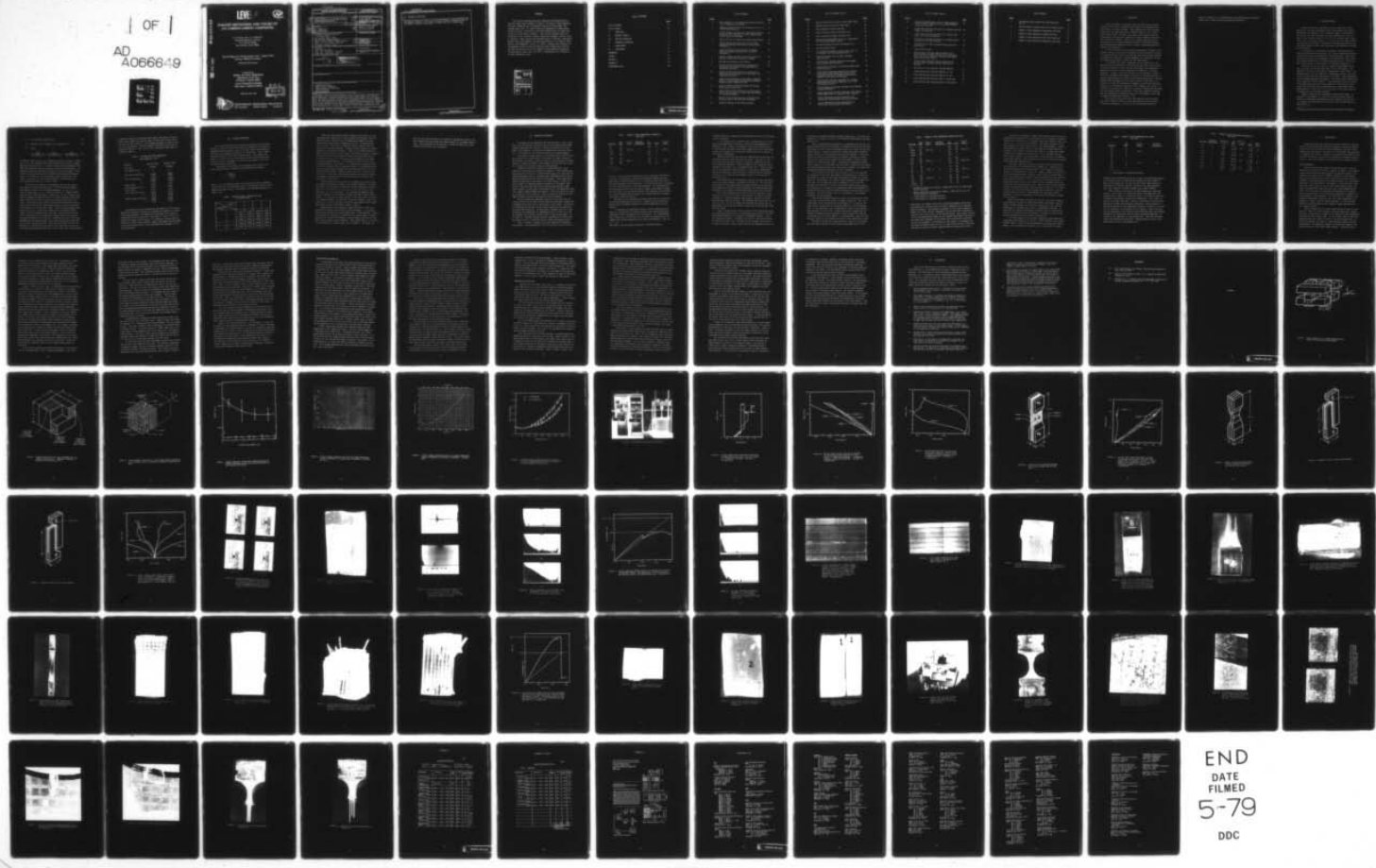
FEB 79 P H FRANCIS, C T ROBINSON

NL

UNCLASSIFIED

SWRI-02-4982

| OF |  
AD  
A066649



END  
DATE  
FILMED  
5-79  
DDC

AD A066649

DDC FILE COPY

LEVEL II

12  
SC

# DAMAGE MECHANISMS AND FAILURE OF 3-D CARBON-CARBON COMPOSITES

P. H. Francis and C. T. Robinson  
Southwest Research Institute  
P. O. Drawer 28510  
San Antonio, Texas 78284

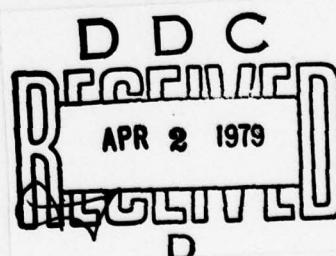
Interim Report for Period August 1977 - August 1978  
Contract N00014-77-C-0510

Unlimited Distribution

Prepared for  
**OFFICE OF NAVAL RESEARCH**  
Department of the Navy  
Arlington, Virginia 22217

**NAVAL WEAPONS CENTER**  
China Lake, California 93555

February 28, 1979



**SOUTHWEST RESEARCH INSTITUTE**  
SAN ANTONIO      CORPUS CHRISTI      HOUSTON

## UNCLASSIFIED

SECURITY CLASSIFICATION OF THIS PAGE (When Data Entered)

REPORT DOCUMENTATION PAGE		READ INSTRUCTIONS BEFORE COMPLETING FORM
1. REPORT NUMBER	2. GOVT ACCESSION NO.	3. RECIPIENT'S CATALOG NUMBER
4. TITLE (and Subtitle) DAMAGE MECHANISMS AND FAILURE OF 3-D CARBON-CARBON COMPOSITES		5. TYPE OF REPORT & PERIOD COVERED Interim Report August 1977 - August 1978
6. AUTHOR(s) P. H. Francis O. T. Robinson		7. PERFORMING ORG. REPORT NUMBER SwRI-02-4982
8. PERFORMING ORGANIZATION NAME AND ADDRESS Southwest Research Institute P. O. Drawer 28510 San Antonio, Texas 78284		9. CONTRACT OR GRANT NUMBER(s) N00014-77-C-0510
10. PROGRAM ELEMENT, PROJECT, TASK AREA & WORK UNIT NUMBERS		11. CONTROLLING OFFICE NAME AND ADDRESS Dept. of Navy, Office of Naval Research ATTN: Dr. A. M. Diness, Director Arlington, Virginia 22217
12. REPORT DATE February 1979		13. NUMBER OF PAGES 87 + prelims
14. MONITORING AGENCY NAME & ADDRESS (if different from Controlling Office) Commander Naval Weapons Center ATTN: Mr. John Patton, Code 3161 China Lake, California 93555		15. SECURITY CLASS. (of this report) Unclassified
16. DISTRIBUTION STATEMENT (of this Report) <i>P. H. Francis</i> Unlimited		17. DISTRIBUTION STATEMENT (of the abstract entered in Block 20, if different from Report) <b>DISTRIBUTION STATEMENT A</b> Approved for public release; Distribution Unlimited
18. SUPPLEMENTARY NOTES		
19. KEY WORDS (Continue on reverse side if necessary and identify by block number) Composite Materials Carbon-Carbon Composites Thermo-mechanical Properties Crack Initiation SEM Fractography		
20. ABSTRACT (Continue on reverse side if necessary and identify by block number) Mechanical property characterization tests were conducted on specimens from a three-dimensional, cartesian orthogonally woven carbon-carbon (C-C) material. Tests consisted of tensile and rail shear, which were conducted at room temperature, and compression tests conducted at room temperature up to 2165°C (3930°F). Stress-strain characteristics and acoustic emission instrumentation were employed to infer the mechanics of the fracture initiation process. In addition, a specially developed axial loading stage integral to SwRI's ETEC scanning electron		

**UNCLASSIFIED**

**SECURITY CLASSIFICATION OF THIS PAGE(When Data Entered)**

20. ABSTRACT (Continued)

microscope facility was used to view and videotape the crack initiation and development processes. As a result of these studies, a tentative model is described to explain the mechanics of failure in 3-D C-C composites.

**UNCLASSIFIED**

**SECURITY CLASSIFICATION OF THIS PAGE(When Data Entered)**

## FOREWORD

The research reported herein was conducted by Southwest Research Institute under Contract N00014-77-C-0510 to the Office of Naval Research. The report summarizes work accomplished during the period August 1977 through August 1978. Dr. Arthur Diness was responsible for ONR program direction, and Mr. John Patton of the Naval Weapons Center at China Lake served as the Navy Project Engineer. The work was conducted under the supervision of Dr. Philip H. Francis, SwRI Project Manager, with Mr. Craig T. Robinson of SwRI carrying the responsibilities of Principal Investigator. Several other staff members contributed importantly to the research effort. Special acknowledgement is due to Dr. David L. Davidson, who conducted the fractographic studies in the SwRI SEM with axial loading stage facility, Mr. Henry Garcia for his work in running the room temperature mechanical characterization tests, and to Mr. Hans J. Muehlenhaupt for carrying out the high temperature tests.

REF ID:	DATA SOURCE
075	DATA SOURCE
080	DATA SOURCE
DEFINING WORDS	
SUBSTITUTION	
<hr/>	
BY.....	
DISTRIBUTION/AVAILABILITY CODES	
<hr/>	
010.	AVAIL. AND/OR SPECIAL
<b>A</b>	

TABLE OF CONTENTS

	<u>Page</u>
LIST OF FIGURES	vi
LIST OF TABLES	ix
I. OBJECTIVES	1
II. MATERIAL SYSTEM	3
III. PHYSICAL PROPERTIES	6
IV. MECHANICAL PROPERTIES	9
V. DAMAGE MODES	17
VI. CONCLUSIONS	27
REFERENCES	29
FIGURES	31
APPENDIX A	79
APPENDIX B	81
DISTRIBUTION LIST	83

## LIST OF FIGURES

<u>Figure</u>		<u>Page</u>
1	Basic Geometry of 3-D Carbon-Carbon Material System with Rectangular Yarn Bundles.	32
2	Schematic Drawing of Unit Cell Structure for 2, 2, 3 Carbon-Carbon Material.	33
3	Cutting Scheme, for Billet No. 2696, Which Produced Mechanical Test Specimens as Well as Density and Thermal Expansion Specimens.	34
4	Density Profile of As-Received Carbon-Carbon Billet.	35
5	Typical Thermal Expansion Curve for the Lower Temperature Ranges as Recorded by a Quartz-Tube Dilatometer.	36
6	Typical Thermal Expansion Profile for Higher Temperature Ranges as Observed in an Optical Dilatometer.	37
7	Complete Thermal Expansion Curves for Both the Z- and the Y-Directions, from 20°C to 2700°C.	38
8	MTS Model 810 Materials Test System.	39
9	Typical Stress-Strain Relations as Measured by Transverse Strain Gages on all Four Sides of a Compression Specimen.	40
10	Typical Stress-Strain Relations as Measured by Longitudinal Strain Gages on all Four Sides of a Compression Specimen.	41
11	Stress-Strain Relations for Two Gages on Opposite Sides of a Specimen Which Exhibited Considerable Bending During a Compression Test.	42
12	Sketch of Typical Tension Specimen with Biaxial Strain Gages on Each Face.	43
13	Typical Stress-Strain Relations for Three Longitudinal Strain Gages (the Fourth Gage Shorted Out) on a Tensile Specimen.	44
14	Sketch of Tensile Specimen with a Reduced Cross-Sectional Area in the Critical Test Region.	45
15	Schematic Drawing of Rail Shear Specimen.	46

LIST OF FIGURES (Cont'd)

<u>Figure</u>		<u>Page</u>
16	Typical Stress-Strain Curves for Rail Shear Tests.	47
17	Loading Sequence During Rail Shear Test.	48
18	Shear Specimen After Test Was Run.	49
19	Pentel 0.5mm Lead Break on Specimen C-24.	50
20	Count Distribution Graph, Specimen C-10.	51
21	Typical Load-Displacement Curve for a Compression Test Under Displacement Control.	52
22	AE Count Distribution Graph for Specimen T-3.	53
23	Acoustic Emission Data.	54
24	Five Channel Recording of AE Data (See Figure 23 for Details) for Shear Specimen (#S-7).	55
25	Typical Phenomenon Seen in Shear Specimens (Specimen S-7).	56
26	Failed Tensile Specimen (Specimen T-6) Showing Very Localized Fiber Fracture.	57
27	Failed Tensile Specimen (T-4) Showing Random Fiber Failure Location.	58
28	Failed Tensile Specimen (Specimen T-4) Showing Longitudinal Fibers Which Have Pulled Out of Surrounding Matrix and Transverse Fiber Bundle Regions, at the End of the Specimen.	59
29	Failed Tensile Specimen (Specimen TT-1) Showing Some Fibers Which Pulled Completely out of the Surrounding Structure.	60
30	Failed Compression Specimen (Specimen C-24) Showing Brooming Phenomenon.	61
31	Failed Compression Specimen (Specimen C-19) Showing Normal Displacement of Transverse Fiber Bundles.	62
32	Failed Compression Specimen (Specimen C-20, Y-Direction) Showing Shear-Like Failure Surface.	63
33	Failed Compression Specimen (Specimen C-11, Z-Direction) Showing Shear-Like Failure.	64

LIST OF FIGURES (Cont'd)

<u>Figure</u>		<u>Page</u>
34	Load Versus Displacement Curve for High Temperature (1930°C, 3500°F) Compression Test, Showing Sudden, Catastrophic Failure.	65
35	Failed Shear Specimen (Specimen S-2) Showing Localized Damage at Pinned Hole.	66
36	Failed Shear Specimen (Specimen S-2) Showing Large Amount of Plastic Deformation.	67
37	Failed Shear Specimen (Specimen S-1) Showing Unusual Phenomenon of "Brittle" Failure.	68
38	Loading Stage for ETEC Autoscan Scanning Electron Microscope.	69
39	Typical SEM Specimen.	70
40	SEM Photograph (Specimen SEM-14) Showing Crack Which Initiated in Shear, Propagated in an Opening Mode, and Finally Turned 90° (to Shear Mode Again) and Ran Along Fiber Bundle.	71
41	SEM Photograph (Specimen SEM-14) Showing Crack Running Across Top Edge and Down Front Face of Specimen.	72
42	Stereo Pair of Crack Network (Specimen SEM-20).	73
43	Failed SEM Specimen (Specimen SEM-20), at 17X.	74
44	Failed SEM Specimen (Specimen SEM-21), at 17X.	75
45	Failed SEM Specimen (Specimen SEM-2, Z-Direction).	76
46	Failed SEM Specimen (Specimen SEM-18, Y-Direction).	77

## LIST OF TABLES

<u>Table</u>		<u>Page</u>
1	Preform Data Sheet Supplied by Fiber Materials, Inc. (2)	5
2	Measured Density Gradient Data for C-C Billet (g/cc)	6
3	Summary of Room Temperature Compression Test Data	10
4	Summary of Room Temperature Tensile Test Data	13
5	Summary of Room Temperature Rail Shear Test Data	15
6	Summary of High Temperature Compression Test Data	16

## I. OBJECTIVES

Since the middle of this decade there has been ever increasing potential for the use of advanced carbon-carbon (C-C) materials in selected areas of defense hardware. These materials have good strength retention at the high temperatures (~3000°C) found in, e.g., rocket nozzle applications. Moreover, they generally have good erosion and environmental tolerance when compared with other comparable materials, such as pyrolytic graphite. However, the complex and unusual microstructural nature of three-dimensionally woven C-C materials demands a more thorough understanding in order to predict thermo-mechanical performance and reliability.

In 1977 the Office of Naval Research established a program of four research projects to provide an integrated focus on problems of mechanical characterization, fracture, processing, and microstructural analysis of advanced C-C materials. Program management was coordinated through the Naval Weapons Center at China Lake (Mr. John Patton).

It is within this program framework that the objectives of the present project were defined. During the one-year effort reported herein, the main objective has been to gain new insight into mechanisms of mechanical failure of a three-dimensional C-C material of cartesian geometry. In order to meet this objective it was necessary to characterize the strength and deformation properties of the chosen material in various loading modes and at ambient and elevated temperatures. Acoustic emission (AE) instrumentation was used in several of the tests in an effort to evaluate the progression of damage by various microstructural sources, e.g., interfacial separation, fiber breakage, and pullout, etc. A series of tests was also conducted in a special loading stage developed for the scanning electron microscope. These tests allowed the observation and videotaping of magnified regions of the specimen in real time as damage developed under monotonic load.

The results of these tests have made possible initial insights into how C-C materials begin to fail under different load states and at various temperatures. As more work is accomplished toward this

project's objectives, it is believed that this newly-acquired knowledge should lead to improved hardware design and reliability.

## II. MATERIAL SYSTEM

The material system investigated in this project was a three-dimensional, cartesian orthogonally woven carbon-carbon (C-C) material supplied by Fiber Materials, Inc., Biddeford, Maine. FMI fabricated two billets, Nos. 2695 and 2696, each being nominally 20.3 cm (8 in.) long in the z direction and 10.15 cm (4 in.) in both the x and y directions. Half of billet No. 2696, i.e., a 10.15 cm (4 in.) cube of material, was used in the present investigation; the remaining material was distributed among the other three contractors\* as prescribed by the NWC Project Engineer.

The precursor for the fibers was HM-3000, a polyacrylonitrile (PAN) yarn manufactured by Hercules, Inc., using a high-modulus process. The matrix precursor was Ashland 240, a petroleum pitch. Each billet was exposed to seven pitch impregnation and carbonization (PIC) cycles, nine graphitization cycles, and three proprietary cycles. Densification routing sheets for these billets are included in Appendix A.

The first PIC cycle is done in a vacuum at approximately 200°C. This cycle gives the billet a good deal of its final rigidity. The 5000 psi PIC cycles are conducted at temperatures of 550 to 600°C. The graphitization cycles are conducted at atmospheric pressure; the first six are at 2600°C and the final three are at 2400°C. These temperatures are the sighted (measured) temperatures. The actual billet temperatures may be some 100° to 120°C higher.<sup>(1)</sup> The proprietary cycles at the end of the fabrication process are very similar to the initial PIC cycle, except that the billet is now impregnated with a resin rather than a petroleum pitch. This type of cycle is typical of the final cycles in the manufacture of propulsion materials.

Figure 1 shows the basic geometry of the material system. An analysis of the geometry of a unit cell of this structure (Figure 2) leads to the following relationships for the volume of the unit cell  $V_c$ , volume of the yarn bundles  $V_y$  in the unit cell, and the fiber volume fraction  $V_f$ :

---

\* Atlantic Research Corporation, UCLA, and the University of Wyoming.

$$V_c = (Y_x + Z_x)(X_y + Z_y)(X_z + Y_z) \quad (1)$$

$$V_y = X_y X_z (Y_x + Z_x) + Y_x Z_z (X_y + Z_y) + Z_x Z_y (X_z + Y_z) \quad (2)$$

$$V_f = V_y / V_c$$

$$= \frac{X_y X_z}{(X_y + Z_y)(X_z + Y_z)} + \frac{Y_x Y_z}{(Y_x + Z_x)(X_z + Y_z)} + \frac{Z_x Z_y}{(Y_x + Z_x)(X_y + Z_y)} \quad (3)$$

The matrix volume fraction,  $V_m$ , assuming the absence of voids, is simply  $V_m = 1 - V_f$ . The expression for  $V_f$  given above indicates that the minimum fiber volume fraction is  $3/4$  and occurs when the yarn bundles in all three directions have the same, square, cross-sectional dimensions. Any deviation from this condition will increase  $V_f$ ; at the extreme, if the fibers in any one direction have vanishing cross-sectional dimensions, then  $V_f = 1.0$ --that is, the yarn bundles occupy the whole unit cell space. In the case of circular yarn bundles of equal diameter, the above expression leads to  $V_f = 3\pi/16 = 58.9\%$ .

In the case of the material system under study in this project, data supplied by Fiber Materials, Inc.,<sup>(2)</sup> from the preform geometry (see Figure 2) leads to the following dimensions:  $X_y = X_z = Y_x = Y_z = 0.071$  cm (0.028 in.);  $Z_x = Z_y = 0.086$  cm (0.034 in.). Based on these data the fiber volume fraction is, from Eq. (3), 75.23%. Another calculation of interest concerns the ratio of the area occupied by the fiber ends to the unit cell area on each of the three principal unit cell faces. These three ratios (one for each principal direction) are identical to the ratios of the fiber bundle volumes, in each of the principal directions, to the unit cell volume. For the present geometry these ratios in the x, y, z directions, respectively, are 0.2258, 0.2258, 0.3007, or in the proportions 30%, 30%, 40%. This means that the density of fiber ends in the z-direction is higher than in the other two principal directions by the ratio 4/3, indicating that (to a first-order approximation) the axial strength in the z-direction should exceed that in the x and y directions by 33%. Note that the areas of the yarn bundle ends are in the ratios 28.8%, 28.8%, 42.4%, and differ from the ratios given above because the unit cell is not a cube, but a parallelopiped.

It should be mentioned that these values differ from those of the supplier, which address the relative number of fiber ends on each side of the unit cell and consider not only spacing and number of ends per site, but also void geometry. The yarn volume fractions for both billets as computed by FMI are: 23.7%, 23.7%, 52.6%. The preform data sheet is included as Table 1.

TABLE 1. PREFORM DATA SHEET SUPPLIED BY  
FIBER MATERIALS, INC. (2)

<u>Property</u>	<u>Mfg. No. 2695</u>	<u>Mfg. No. 2696</u>
Yarn Type	HM-3000	HM-3000
Yarn Ends/Site x,y	2	2
z	5	5
Yarn Bundle Spacing x,y	0.056"	0.056"
z	0.062"	0.062"
Preform Dimensions x	4.265"	4.290"
y	4.288"	4.289"
z	8.521"	8.571"
Weight (gms)	2073	2078
Preform Density (g/cc)	0.812	0.803
Fiber Volume	43.9%	44.4%
Yarn Volume Fractions x	23.7%	23.7%
y	23.7%	23.7%
z	52.6%	52.6%
Reinforcement Fractions x	10.9%	10.9%
y	10.9%	10.9%
z	24.1%	24.1%

The material system described above was chosen as a first step in gaining the experience necessary for studying the behavior of cylindrically woven materials. The geometry and processing of the material system used in this research were very similar to those currently employed in strategic rocket nozzles. By choosing a cartesian material system for initial characterization, smaller and simpler specimen geometries could be used, which in turn facilitated the assessment of the observed behavior.

### III. PHYSICAL PROPERTIES

One of the concerns about the physical properties of the present billets, as well as of in-service billets, is whether or not there are substantial density gradients and, if so, what effect these gradients may have on the mechanical properties of the material. Table 2 shows tabulated results of four sets of density tests. Test samples were cubes, 1.3 cm (0.5 in.) on a side taken at points spaced equally from near the surface to the middle of the billet (see Figure 3 for exact locations within the billet).

The weights of the samples were determined both in and out of water, and the density calculated per ASTM D792 specifications:

$$\rho = \frac{0.9975}{1 + \frac{W_o - W_w}{W_a}} \quad (4)$$

where:  $W_o$  is the apparent weight of the wire hook partially immersed in the water,  $W_w$  is the apparent weight of the specimen, with wire hook, immersed in water, and  $W_a$  is the weight of the specimen (without wire hook) in air.

TABLE 2. MEASURED DENSITY GRADIENT DATA FOR  
C-C BILLET (g/cc)

Measurement No.	Specimen No.	1	2	3	4
1	1.9167	1.9238	1.8940	1.8982	
2	1.8979	1.8782	1.8768	1.8709	
3	1.9071	1.8743	1.8666	1.8691	
4	1.8966	1.8725	1.8738	1.8689	
$\bar{x}$	1.9046	1.8872	1.8778	1.8768	
S.D.	0.0093	0.0245	0.0116	0.0143	

Since the carbon-carbon material system is quite porous, it was anticipated that absorption of water during the tests might affect the density results. Thus, each of the samples was weighed four times, allowing three days between weighings to dry out. As seen from the data in Table 2, there was no consistent trend to absorb and retain water with successive weighings. Graphical results showing the density gradients are presented in Figure 4. There is a definite density gradient from the surface into the center of the billet; however, it should be noted that the total variation in density from the billet edge to the center was only 1.5%. The scale has been enlarged in the figure to show the gradient better. The standard deviation for each set of four measurements is also shown. It is likely that a density gradient of this size would not have an important effect on the mechanical properties of the material, although this statement would have to be verified by further testing. However, during the course of the tests on this project, there was no noticeable difference in mechanical properties between specimens taken from the billet surface and those from the center of the billet.

Another physical property which is of importance in applications of carbon-carbon material systems is the thermal expansion. Six specimens (three in the z-direction and three in the y-direction), 0.635 cm x 0.635 cm x 5.08 cm (0.25 in. x 0.25 in. x 2 in.), were sent to Fiber Materials, Inc., to be evaluated. Each specimen was measured with a quartz dilatometer in the temperature range from 20°C to 850°C (68°F to 1560°F). In each case, the data tracked a continuous curve; see Figure 5 for a typical example. As expected, the material showed a slight contraction, in each case reaching a minimum at approximately 350°C (660°F). Upon further heating, the material began to expand.

Measurements in the temperature range from 350°C to 2700°C were made with an optical (twin telemicroscope) dilatometer. A continuous plot was not possible, since measurements must be taken manually. Results for this part of the tests are typified by the results shown as Figure 6. The data for the optical dilatometer contain somewhat more scatter than those from the quartz tube dilatometer. The results from all of the tests are superimposed on a single master plot in Figure 7. The single fit

curve for each fiber direction is a visual fit through the curves at the lower temperatures and through the discrete points at the higher temperatures. Total expansion of the material at 2700°C was about 0.9% in the z-direction and 0.6% in the y-direction.

#### IV. MECHANICAL PROPERTIES

The purpose of the mechanical tests was two-fold: first, to produce a set of mechanical properties data for the material under simple loading conditions; and, second, to observe and analyze the failure modes of the material. The mechanical properties are discussed below, and a description of the failure processes is provided elsewhere.

The complete cutting scheme for the original billet, half of which was provided for the SwRI phase of the program, is shown in Figure 2. All specimen types were cut from the billet so that half would be tested along the z-direction (thicker fiber bundles) and the other half along the x- and/or the y-direction (smaller fiber bundles).

Mechanical tests were conducted on an MTS model 810, servo-hydraulic, closed-loop test system; see Figure 8. Since carbon-carbon materials tend to behave in a rather brittle manner, the tests were run under displacement control. Specimens were instrumented with acoustic emission pickups and a full array of strain gages. Strain gage and AE setups are described in more detail in a later section. Strain data were recorded on a Memodyne digital recorder with a 20-channel capability. Data were then taken from the digital tape through a Datel LPR-16 cassette recorder which introduced the data (in hexadecimal form) into a Hewlett-Packard 9830A mini-computer. Data were reduced and stored on a floppy disc for further use. Data could then be plotted on an HP 9862A calculator plotter interfaced with the mini-computer.

For the tension and compression results, it was found that the initial portion of the stress strain curves was sufficiently linear that a straight line could be fit to the points in this region. The slope of the resulting fit was taken as the elastic modulus of the material in the given fiber direction. In cases where a straight line fit to data is assumed, the coefficient of determination ( $R^2$ ) for the fit is used as a measure of how closely the data track a linear relationship. An  $R^2$  value of 1 (or 100%) indicates perfect compatibility of data points and linear fit;  $R^2 = 0$  indicates that no linear relationship exists.

Table 3 presents a summary of the room temperature compression test results. The specimens were 1.27 cm x 1.27 cm x 2.54 cm (0.5 in. x

TABLE 3. SUMMARY OF ROOM TEMPERATURE COMPRESSION TEST DATA

<u>Specimen</u>	$\sigma_{max}$ (MPa)	$\bar{x} + S.D.$ (MPa)	<u>Specimen Orientation</u>	E (GPa)	% Fit	$\bar{x} + S.D.$ (GPa)
C1	155			176	94	
C2	176	176 ± 18	z	---	--	163 ± 11
C2A	173			160	73	
C3	199			154	--	
C14A	101			66	--	
C15	101	103 ± 3	x	68	--	66 ± 2
C16	106			65	87	

<sup>1</sup>  $l_0 = 2$  in.

0.5 in. x 1 in.), with the exception of No. C-1, which was 5.08 cm (2.0 in.) long. A comparison of the data for different compression tests shows that the elastic modulus for C-1 is slightly greater than that of the other specimens in the z-direction. It is also noted that the strength of C-1 is lower than that of the other specimens. The variations from the experimental mean of both the elastic modulus and ultimate strength are very close to the standard deviation of the sampling of test results. It is thus concluded that the longer test configuration had no significant effect on the test results.

The data for the compression specimens taken from the y-direction of the billet showed much less scatter. Results for both the elastic modulus and the ultimate strength in the three samples were very consistent.

In comparing the compression results in the two different directions, it is noted that the elastic modulus in the y-direction was approximately 40% of the modulus in the z-direction. The corresponding fiber volume ratio is 45%\*, and since the fibers are expected to be the primary load carrying components, this result is reasonable. Also, the

\*See Table 1 and the related discussion in "Material System."

ultimate compressive strength in the y-direction was 40% of the strength in the z-direction.

It is pertinent here to mention that at present there is no satisfactory micromechanical constitutive theory for three-dimensional C-C materials. Such a theory, if available, would enable the prediction of the composite strength and stiffness properties from the constituent properties, although these constituent properties were not measured in the present investigation.

Another noteworthy result from the compression tests was that the transverse strains in all cases were very small. They were so low, in most cases, that they were below the resolution capabilities of the data acquisition equipment. Figure 9 shows all four transverse strain readings for specimen C-1 on an expanded strain scale. Figure 10 shows one of the transverse strains plotted on a scale with a longitudinal strain for comparison. Since this was a consistent result throughout the tests, it is concluded that Poisson's ratio for the material is practically zero.

One problem that was encountered in some of the early compression tests was specimen bending, as indicated in Figure 11. The two strain curves shown are from gages mounted on opposite sides of the specimen. This problem was solved by better alignment of the fixturing and closer tolerances in the degree of parallelism between ends of the specimens.

The tension specimens were 10.16 cm (4.0 in.) long with a cross section 2.54 cm (1.0 in.) wide by 0.635 cm (0.25 in.) thick, as shown in Figure 12. Beveled fiberglass tabs served to transfer the loads from the grips into the specimen. The resulting test section was 2.54 cm (1.0 in.) long. As in the compression specimens, one lateral and one longitudinal strain gage were placed on each face of the specimen within the test length.

Figure 13 shows typical curves for three of the longitudinal gages (the fourth gage shorted out) on a specimen oriented in the y-direction. The agreement among all of the gages is considered excellent. As for the compression samples, a straight line was fit to the initial portion of the stress-strain curve. The data fit the straight line very well in nearly every case. Again, as was found in the compression tests, the

transverse gages showed negligible Poisson contractions. Also shown, for comparison, in Figure 13 is one of the transverse stress-strain relations (Channel 14).

From a micromechanical description, an examination of the unit cell geometry shows that each yarn bundle is in physical contact with one other yarn bundle in each of the two orthogonal directions, as well as with two matrix pockets. A tensile loading will therefore introduce transverse tensile strains in the orthogonally-directed yarn bundles. If the yarn bundle can sustain the transverse strain without splitting or without separation at the interface between two yarn bundles in contact, there should be a global Poisson effect. There being no significant Poisson effect, however, it is concluded that splitting of transverse yarn bundles or interface separation may occur under tensile loading. The effect upon subsequent mechanical performance, if any, is unknown.

In reviewing the tensile results in Table 4, it can be seen that the direction of the thick fiber bundles (*z*-direction) has an effect on the mechanical properties even when the specimen is tested in a weaker direction. Specifically, the average tensile strength of specimens T-9, T-10, and T-11 is higher than that of specimens T-6, T-7, and T-8. Specimens T-9 through T-11 have the thick fiber bundles going through the thickness (i.e., normal to the specimen surfaces) and specimens T-6 through T-8 have the *z*-direction fibers oriented across the width of the specimens. The elastic moduli vary in a like manner to the strength properties in this instance.

The tensile specimens having the letter R in parentheses in Table 4 each had a reduced cross-section, as shown in Figure 14. This was done because in the original tests of specimens T-1, T-2 and T-3, the fibers were so strong that the specimens pulled out of the fiberglass tabs. In the subsequent tests of specimens T-2 and T-3, the specimens again sheared out of the tabs. It must therefore be assumed that the ultimate strengths for these specimens are not accurate, but that the calculations for the elastic modulus are representative, since the shear failures occurred in the nonlinear portions of the stress-strain curves.

Specimen T-12 also had a reduced section. Since it was presumed that the reduced sections in the *z*-direction specimens (T-1 to T-4)

TABLE 4. SUMMARY OF ROOM TEMPERATURE TENSILE TEST DATA

<u>Specimen</u>	$\sigma_{\max}$ (MPa)	$\bar{x} + S.D.$ (MPa)	<u>Specimen Orientation</u>	E (GPa)	% Fit	$\bar{x} + S.D.$ (GPa)
<sup>1</sup> T1	126			138	98	
<sup>1</sup> T2(R)	153	<sup>1</sup> 150 $\pm$ 26	z	140	82	154 $\pm$ 18
<sup>1</sup> T3(R)	138			174	97	
T4(R)	185			166	--	
TT1	331			174	100	
TT3	302	<sup>2</sup> 297 $\pm$ 37	z	122	78	140 $\pm$ 29
<sup>2</sup> TT4	257			125	98	
T6	98			57	100	
T7	93	96 $\pm$ 3	<sup>3</sup> y	41	99	48 $\pm$ 8
T8	93			47	100	
T9	128			61	99	
T10	128	128 $\pm$ 13	<sup>4</sup> y	68	100	63 $\pm$ 10
T11	112			50	97	
T12(R)	145			72	97	

1 - slipped or sheared out of grips:  $\sigma(\max)$  and  $\bar{x} \pm S.D.$  for data group may be inaccurate

2 - machine malfunction caused early failure:  $\sigma(\max)$  and  $\bar{x} \pm S.D.$  for data group may be inaccurate

3 - x yarn bundles in thickness direction

4 - z yarn bundles in thickness direction

would affect the results, one of the y-direction specimens (T-12) also was tested with a reduced section to allow a comparison of the measured tensile strengths. The mechanical properties of T-12 can be compared to those of T-9, T-10, and T-11 (specimens with the same fiber orientation) to get an idea of the effect of the reduced section. The ultimate strength of T-12 was significantly higher (by two standard deviations) than that of the other three specimens, but the moduli were statistically equivalent for all four specimens. On the basis of this result, it is assumed that the tensile strength values for T-2, T-3, and T-4 will be 15% to 20% high, and that the values for elastic modulus should be reasonably accurate.

In an effort to develop a tensile fiber failure in the z-direction, specimens TT-1 through TT-4 were machined to have a thickness of approximately 0.318 cm (0.125 in.), or two unit cells, and a width of about 1.27 cm (0.5 in.). As can be seen in Table 4, the tensile strengths of the thin specimens are almost double those of the thicker samples. However, the difference in elastic moduli is less than one standard deviation, leading to the tentative conclusion that there is no significant change in modulus with changes in specimen size. It is concluded from the above results, however, that the strength of this material is dependent on specimen dimension. More insight into effects of scale will be gained during subsequent investigations.

Rail shear tests were conducted to produce shear loading along a plane parallel to the loading direction (Figure 15). Strain gages for the shear specimens were aligned parallel to the loading axis, perpendicular to the loading axis, and at 45°. Figure 16 shows a typical plot of all six strain readings. Channels 2 and 8 (noted on curves) are at 90° to the loading axis, channels 4 and 10 are parallel to the load axis, and channels 6 and 12 are at 45°. As can be seen, the deformation is highly nonlinear, and it is not possible to fit a straight line to any portion of these stress-strain curves. Thus, the only results tabulated are for the ultimate strength; these are given in Table 5. It is interesting to note that shear planes perpendicular to both the y- and the z-fiber directions failed at approximately the same stress levels. Apparently, the fiber strength has little effect on the shear strength of this material.

The most remarkable phenomenon in the shear tests was the amount of deformation the material could sustain before fracturing. Figure 17 shows a loading sequence of specimen S-2, beginning at zero load and progressing to a maximum shear stress of approximately 2500 psi. At this point the inelastic deformation continued, but the load-carrying ability of the material began to decrease. As shown in Figure 18 the residual deformation in the specimen is substantial.

The final mechanical test sequence consisted of high temperature compression tests which were to be run at 1370°C (2500°F) and at 2760°C (5000°F) inside a Centorr Model M60-3X8W-WM-2-25 environmental chamber. However, test conditions necessitated use of a larger set of heating

TABLE 5. SUMMARY OF ROOM TEMPERATURE RAIL SHEAR TEST DATA

<u>Specimen</u>	<u>max (MPa)</u>	<u><math>\bar{x} + S.D.</math> (MPa)</u>	<u>Specimen Orientation</u>
S1	14		
S2	17	15 $\pm$ 2	z
S3	14		
S4	--		
S5	--		
S6	11	14 $\pm$ 4	$l_y$
S7	17		
S8	--		

1 - z yarn bundles in thickness direction

elements than had previously been used at SwRI, and the maximum temperature attainable with the large heating element was 2200°C (4000°F). Even at this temperature, hot spots in the furnace caused warping of some portions of the heat shields. Therefore, the high temperature tests were conducted at 1370°C (2500°F) and at 1930°C (3500°F).

Table 6 shows a tabulation of the high-temperature compression results. Also listed, for comparison with the room temperature compression data in Table 2, are the mean values. It should be noted that, in general, the strength increases with temperature. This result is seen for both fiber directions. However, the stiffness of the material appears to decrease with increasing temperature. The calculation of the elastic modulus at high temperature involved a correction to account for the compliance of the machine and the fixturing. When a test was run, the compliance of the machine and the fixturing, which was measured separately, was subtracted from the apparent specimen compliance, resulting in the compliance for the specimen only. From this compliance value, the stiffness was calculated. Although sound in theory, this method admits room for experimental error.

TABLE 6. SUMMARY OF HIGH TEMPERATURE COMPRESSION  
TEST DATA

<u>Specimen</u>	<u>Specimen Orientation</u>	<u>Temperature (°F)</u>	<u><math>\sigma_{max}</math> (MPa)</u>	<u>Mean <math>\sigma_{max}</math> (MPa)</u>	<u>E (GPa)</u>	<u>Mean E (GPa)</u>
C-6	z	2500	157		15	
C-7	z	2500	168	162	18	16
C-19	y	2500	118		7	
C-20	y	2490	122	120	9	8
C-11	z	3540	198		13	
C-12	z	3530	209	204	13	13
C-21	y	3520	160		9	
C-22	y	3930	---	152	6	8
C-23	y	3550	143		10	

## V. DAMAGE MODES

Damage mechanisms were observed using three different procedures: acoustic emission monitoring during the mechanical tests gave valuable insights into the initiation of failure mechanisms; post-test failure analysis gave a more direct indication of failure modes; and observation of specimens under load in a scanning electron microscope (SEM) allowed real-time observation of initiation of progression of damage leading to failure. These three methods of observation will be discussed in turn.

### Acoustic Emission

Acoustic emission (AE) signals were monitored with a 0.635 cm diameter by 0.238 cm thick (0.25 in. diameter x 0.0938 in. thick) PZT-5 crystal, mechanically pressure-coupled to the specimen surface. The transducer was found to have a resonant frequency of about 200 KHz. Data for the compression tests and for many of the tension tests were displayed in bar graph format by the system recorder. As a preliminary indication of the appearance of the signals, a 0.5 mm lead from a lead pencil was broken on the surface of one of the specimens; Figure 19a shows the resulting RF signal and Figure 19b is the accompanying bar chart. The horizontal axis represents the magnitude of the signals, and the vertical axis is a log scale which represents the number of recorded signals at each magnitude. Note that there are a number of low amplitude "background" counts at four of the lower amplitudes and a reading at a single, distinct, higher amplitude. It was discovered during the actual testing that the signals of higher amplitude also had a longer duration.

Figure 20 shows three of the bar charts during the test of specimen C-10. This is a typical sequence of AE data taken from a compression test. Figure 20a is a display of the cumulative counts immediately following the first audible noise. As can be seen, there is some small amplitude noise and a number of counts at an isolated high level. As the test progressed, the number of lower amplitude signals increased substantially. The high-level signals also became more numerous, and signals from many of the higher ranges appeared. Figure 20b shows a

cumulative count of maximum load for this test. This pattern of numerous low-level counts, decreasing with increasing amplitude (with a small increase in quantity of the highest amplitude ranges), was found to be typical of all of the tests. Figure 20c shows the cumulative display at the end of the compression test. This is not a true indication of the AE pattern after a test, for reasons discussed below; but it does give some indication as to the significance of the signals of different amplitudes. Figure 20b is considered an accurate indication of the AE pattern developed during a test, since it is the pattern immediately following the peak load on the specimen.

Figure 21 shows a typical load vs longitudinal displacement plot for a compression test. There was a major drop in stress at, or perhaps just below, the maximum stress a specimen could sustain. This drop in stress was usually accompanied by a corresponding drop in strain, since the onset of damage usually occurred at the ends of the specimen where the load was applied. This drop coincided with the first large audible cracking noise and resulted in a cumulative AE count as shown in Figure 20a. Following this unloading phenomenon, the specimens again began to accept increasing loads. During this reloading period, significant additional low-level AE signals and a substantial number of intermediate-level signals were recorded. It was, in general, a very quiet period for acoustic noise in that little or no high-level AE signals were recorded. The stress level reached just prior to the first breakdown was usually just below the maximum stress attained in any given test. Upon the first reloading, the peak stress was attained and was immediately followed by a second loud audible crack. Once again, the audible crack coincided with a significant number of high-level acoustic signals (Figure 20b). In most cases the subsequent cycles of reloading did not reach peak stress, but declined steadily. At this point the specimen was considered to have failed. The subsequent cycles emitted much softer audible noise, and during these reloadings many more counts were recorded in the intermediate levels of the AE plot. By the end of the test the cumulative plot of all AE signals looked similar to Figure 20c.

In the period following the second load decrease, it was noticed that the specimens began to spall (brooming phenomenon) at the top or

the bottom surface of the specimen. The specimens would then continue to break down through this mechanism until the test was terminated. It was concluded that this process resulted in the intermediate-level AE signals because the longer a compression test ran, the more intermediate counts would be recorded. This phenomenon probably had no effect on the measured mechanical properties since it occurred very late in the test sequence.

The same acoustic emission monitoring process was used for most of the tension tests, and the results were very similar, as seen in Figure 22. Figure 22a shows the cumulative AE count at 134 MPa (19.4 ksi) stress. This was very early in the test, and the only signals were low-level noise. Figure 22b shows the cumulative AE spectrum after the first loud audible crack was heard. It is presumed that the counts at the single high amplitude were from fiber breakage. Finally, Figure 22c shows the AE accumulation at the end of the test. At the end of the tension test the low-level noise had filled in somewhat, and high-level signals had been recorded at several different amplitude ranges. In contrast to the AE accumulation at the end of the compression tests, low- and medium-amplitude signals were much less numerous in tension. This was probably due to the fact that the compression test had no definite failure point, and as the tests continued, the specimens began to crumble and spall at the ends.

A second method of logging the AE data was used for several tension tests and for two of the shear tests. Figure 23 shows the results for Specimen TT-3. Beginning with the bottom channel, the first channel is load: full scale is 5000 lb, which corresponds to an applied stress of 539 MPa (78 ksi). The second channel is a simple count rate of all counts above a 10 mV threshold, with a full scale of 5V. The third is a blank channel. The fourth, fifth, and top channels are accumulated ring-down counts with respective thresholds of 400 mV, 100 mV, and 10 mV. Full scale for these three channels is 65,536 counts.

It can be seen that the first significant acoustic noise occurred when the load curve showed the first drop. The count rate registered a substantial amount, and the accumulated ring-down counts for 10 mV and 100 mV thresholds increased noticeably. The acoustic noise then abated until the load curve approached the point at which it began to

level out. At this time the acoustic emission again increased, and substantial increases were recorded in all three ring-down accumulations. The increases continued until catastrophic failure of the specimen.

Similar data for a shear test are shown in Figure 24. As the load increases, the AE activity increases up to a point, then it appears to remain constant. Increased AE activity is observed just before peak load and again just as the load begins to decrease. The activity as load begins to decrease appears to be the most significant of the entire test. Later in the time sequence there is a more rapid decrease in load carrying ability of the specimen. This event is marked, not by increased noise during (or just prior to) the load drop, but by a temporary lull in the AE activity following the drop. This is presumably due to the stress redistribution within the material, before the load again begins to increase. There is a final burst of activity at the end of the test, but it is thought that this was due to the specimen shearing out of the rail fixtures. Evidence of this is seen in Figure 25, which shows a pinned hole which sheared out at the end of the test.

Due to the constant, moderate intensity, AE activity during the shear tests and the extreme amount of deformation during these tests, it is presumed that an accumulated count of signals within given amplitude ranges (as described for compression and earlier tension tests) during the shear tests would show a great deal of low- and intermediate-level signals and very few high-amplitude signals.

Based on the above observations, it was concluded: (1) that the AE signals of lower amplitude could be attributed to failure (crumbling or shearing) of the matrix material; (2) that the intermediate-amplitude signals were due in part to fiber crippling during stress redistribution, but perhaps more significantly to the "brooming" (spalling) failure encountered in the later stages of the compression tests; and (3) that the high-level signals were associated with sudden fiber failure. The consistency of these results lends a great deal of credibility to acoustic emission as a method of monitoring the mechanical integrity of carbon-carbon composites under applied loads.

### Post-Test Failure Analysis

In analyzing the specimens after they had failed, it was noticed that the orientation of the strong fiber direction had significant influence on the mode of failure. Figure 26 shows the failure surface of specimen T-6. The thick fiber bundles are oriented across the width in this case, and the fiber bundles broke off straight across the specimen. There was very little, if any, apparent shear between the fibers and matrix regions. In contrast, specimen T-4 (Figure 27), in which the strong fiber direction is along the loading axis, showed a much greater tendency for the fibers to shear out of the matrix rather than fail in a tensile mode. There is presumably a great deal of shear deformation since the fiber bundles failed at different locations. If there were no shear deformation, the fiber bundles would all tend to fail along the same plane since a local failure of one bundle would cause a stress concentration and redistribution in the same region. However, the seemingly random locations of fiber bundle breakage indicates that substantial shear deformation may have distributed the stress concentrations along the test length. A direct indication of the shear during the tensile tests can be seen in the end of specimen T-4 (Figure 28). It is obvious that the longitudinal fiber bundles have pulled away from the transverse fiber bundles, even though all of the fibers failed within the test length of the specimen (refer back to Figure 27). Further examples of the shear deformations were seen in the tests of the thin tensile specimens (Figure 29). In many of these tests, in which the specimens were only two unit cells thick, some of the fiber bundles pulled completely out of the supporting structure without breaking.

Several interesting phenomena were observed during post-test examinations of the compression samples. The most obvious damage was a "brooming" effect (Figure 30). As mentioned earlier, this effect became obvious after the specimen had ceased to carry peak load. It is not believed that this damage mechanism had any effect on the ultimate strength, but once the specimen began to crumble in this manner, it continued doing so at a lower load than was required to initiate the process. This brooming phenomenon was found in specimens oriented in both the y- and z-directions.

Another characteristic that was noticed in many of the failed compression specimens was that some of the weak (i.e., x or y) fiber bundles on the free surface oriented perpendicular to the loading direction tended to be squeezed out of position, almost to the stage of being sloughed off (Figure 31). The specific time at which this event occurred was not noted. Thus, it is not known if it was due to Poisson strains or was a result of the buckling or crippling of interior fiber bundles. It is possible that one or more longitudinal fiber bundles at a location just under the surface could buckle and outwardly push a lateral bundle which was originally at or near the surface, thus giving the observed result. This deformation of lateral fiber bundles was observed in tests at all temperatures, and in both the y- and z-orientations. Like the brooming-type damage, this lateral displacement mode was noticed only in the later stages of strain: i.e., after the specimen had ceased to support the peak load and had begun visibly to fail.

There was one failure mechanism that was noticed only in some of the high-temperature compression tests. Specimen C-20, oriented in the y-direction and tested at 1370°C (2500°F), showed an oblique fracture surface (Figure 32) much like a conventional shearing-mode failure. Specimens C-11 (Figure 33) and C-12, oriented in the z-direction and tested at 1927°C (3500°F), also failed through a shearing mode. The test of specimen C-11 was stopped before complete failure. The angle of the failure surface, in all three cases, was approximately 25° to 30° from a plane normal to the loading direction.

Characterization of the stress-strain curves for the compression tests indicates that most of the specimens failed gradually with increasing load. However, specimens C-11 and C-12 failed suddenly and catastrophically as shown in Figure 34. Even though C-20 had an oblique failure surface, it did not fail catastrophically as did C-11 and C-12. It appears that the higher temperatures have a tendency to render the matrix material somewhat stronger and more brittle. This would explain the shear-mode failure surfaces and the more sudden failures as well as the slightly higher compressive strengths at the high temperatures.

The shear specimens, in most cases, sheared out of the pinned grips (Figure 35) before they failed along the intended slip plane. As mentioned in the previous section, there was substantial elastic

and plastic deformation in these specimens. Figure 36 shows a shear specimen after a test. The amount of permanent deformation is readily visible. The only specimen which did not behave in this manner was S-1, which failed suddenly and in a brittle fashion (Figure 37). The reason for this seemingly erratic behavior is not known. It should also be noted that the compressive strength of S-1 was right at the mean value for the five valid shear tests. Thus, whatever the cause of the brittle behavior, it did not seem to affect the strength of the material.

#### Observations in the SEM

Observation of specimens, under load, in a scanning electron microscope (SEM) proved to be a most valuable method of describing damage modes from initiation to final failure. SwRI's ETEC Autoscan SEM has been fitted with a load stage capable of applying tensile loads up to 4450 newtons (1000 lb) force. The details and capabilities of this specially designed load stage are given in Appendix B. Figure 38 shows the loading stage with one of the carbon-carbon specimens.

The load-carrying mechanism for this loading facility consists of two pins at the edges of each end of the specimen (Figure 39), and a specimen must have a suitable shear strength to distribute the load across the specimen and through the test section. Previous tests had shown that the carbon-carbon material did not itself have a sufficient shear strength; therefore, aluminum tabs were bonded to the specimens to facilitate the shear transfer.

All of the SEM specimens were machined with a reduced cross-section as shown in Figure 39. This was done to localize the damage initiation so that it could be observed in the limited area covered by the electron beam at any given instant. Also, some of the specimens were notched to localize damage initiation even more.

Upon observing several of these specimens it became apparent that damage initiated in a shear mode in many cases. Figure 40 shows a crack which initiated due to slip between a yarn bundle and a matrix region. It should be noted that the fibers were oriented at an oblique angle to the specimen surface due to the shape of the test section (constant radius reduction), and this configuration would obviously have had an influence on the initiation mechanism. Figure 41 shows a similar crack

running across the top edge and down the front face of specimen SEM-14. The overall crack configuration indicates that the initiation occurred in a sliding mode. (The loading is outward in a horizontal direction for all figures unless noted otherwise.) Once again the initiation was apparently due to the slip between a yarn bundle and a matrix pocket, yet the crack actually developed in the matrix region adjacent to the yarn bundles rather than at the fiber-matrix interface.

Another specimen configuration which showed an apparent shear-mode initiation was a notched specimen. Figure 42 presents a matched stereo pair of a damaged region under a notch. Under a stereo viewer, the effect of the horizontal (x-direction) displacement difference between a loaded and unloaded specimen can be seen as a topographic (z-direction) effect. This phenomenon is described in Reference 3. It is apparent that the damage initiated in a shear mode between the fiber and matrix regions proceeding in both directions from the notch root. The crack to the left abruptly changed to an opening mode crack (turned almost straight down), while the crack on the right proceeded along the interface region for some distance before slowly turning perpendicular to the loading direction (downward).

The crack network in Figure 42 gives a fairly good indication of the general pattern of crack growth in this three-dimensional material. The cracks, on either side of the notch, originated in a shear mode in the proximity of a fiber-matrix interface, and then changed, with varying speeds, to opening mode cracks. The crack on the left changed very abruptly to a direction perpendicular to the applied load, and the crack on the right curved very slowly, never actually reaching a point where it had changed directions by a full 90°.

Both cracks, as they progressed through the matrix region, favored running through the larger voids present, even when the voids were somewhat out of the path of the crack. As the propagating cracks approached other longitudinal yarn bundles (lower regions of Figure 42), they again changed directions and proceeded along the interface region, parallel to the longitudinal bundles. As the cracks continued to propagate along the longitudinal yarn bundles, they encountered no apparent difficulty in shearing through the transverse yarn bundles. That is, cracks propagating in a shear mode near the fiber bundle/matrix interface favored

shearing through transverse bundles as they were encountered, rather than arresting or redirecting themselves in the mode 1 direction. This result is further evidence that the yarn bundles, as well as the matrix material, are very weak in shear.

A typical crack pattern for a single crack is found in Figure 40. Initiation was at a shoulder where the yarn bundle and matrix region developed considerable shear stress (top of photo). The crack then turned rather abruptly from shear mode to opening mode (horizontal to vertical orientation) and propagated through the matrix region until it approached a longitudinal yarn bundle. At this time it turned back to a direction parallel to the yarn bundle (shearing mode) and propagated along this direction until the specimen failed.

Failure of the SEM specimens appears to have developed by the same mechanisms as failure of the tensile specimens. In many areas of the specimen, yarn bundles would shear out of the matrix so that the fiber failure would not be at the same location as the matrix failure. Note in Figure 43 that the matrix regions have failed directly beneath the notch, but the two lower yarn bundles (the upper bundle was cut when the specimen was notched) apparently failed at another location. In specimen SEM-21 (Figure 44), which was also notched, the yarn bundles all failed directly below the notch, but the matrix failure occurred as far as one-quarter inch away from the fiber failure. In specimen SEM-24, the matrix failure was all directly below the notch and much (but not all) of the fiber failure was in the same vicinity.

In some of the specimens which failed completely, the yarn bundles pulled completely out of the specimen without fracturing. This failure mechanism was not limited to any one particular orientation. Figure 45 shows a z-direction specimen in which the fibers pulled out of the matrix, and Figure 46 shows a y-direction specimen in which most of the longitudinal yarn bundles remained unbroken.

The conclusion from the above discussion is that the fiber breakage, when it does occur, is of a rather random nature reflecting the highly redundant structure of the material system. The location of fiber fracture seems to depend on weaknesses in individual bundles rather than any stress concentration due to notches or other physical characteristics. In this respect, this material could be considered to

be insensitive to notches. However, the notches do help facilitate differential shear strains which lead to the initiation of the damage mechanisms. The other characteristic which facilitates high shear stress (and therefore strains) is the compliance of the matrix material compared to the fibers. The yarn bundles seem to be much stiffer (in the fiber direction) than the matrix pockets.

It was mentioned earlier that as shear cracks propagate along longitudinal yarn bundles, a crack develops in the matrix material in the immediate vicinity of the matrix-fiber interface. The same phenomenon was noticed between the transverse bundles and matrix regions as cracks developed in an opening mode (vertical cracks in Figures 43 and 44). The more nearly square regions on the faces of these specimens are the ends of z-direction fiber bundles. The thinner rectangular regions, with larger apparent voids, are matrix pockets. It was thought that the cohesion between fibers in a bundle would not be very strong. However, when opening cracks developed, they developed in the matrix regions immediately adjacent to and parallel to the fiber bundles. Thus the fibers appear to have a bond between them that is stronger than the matrix material.

## VI. CONCLUSIONS

Efforts were made during this project to describe failure initiation processes in a three-dimensional Cartesian orthogonally woven C-C material. The billet used in this investigation, supplied by Fiber Materials, Inc., of Biddeford, Maine, used HM-3000 fibers, had a density of 1.89 and was constructed with yarn volume fractions of 23.7%, 23.7%, 52.6%. The conclusions presented below are based on measurements and observations regarding physical and mechanical behavior, as well as damage initiation, made during this exploratory effort.

1. Density gradients appear small: a decrease of 1.5% in density was measured from the surface to the center of the 10.15 cm (4 in.) billet cube.
2. The thermal expansion is a minimum (and slightly negative) at about 350°C. At higher temperatures it increases, with the z-direction expansion some 50% greater than that in the transverse directions; e.g., at 2700°C  $\alpha_x = \alpha_y = 2.2 \times 10^{-6}/^{\circ}\text{C}$  and  $\alpha_z = 3.3 \times 10^{-6}/^{\circ}\text{C}$ .
3. Results from room-temperature tension and compression tests indicate that the Poisson ratios are virtually zero.
4. Compression strength increases with temperature: e.g., specimens of both y and z orientations showed a 26% strength increase from 1370°C to 1930°C (2500°F to 3500°F). The compression modulus, however, decreases markedly with increased temperature. At high temperatures the matrix material appears to have more strength and to become more brittle than at room temperatures.
5. Tensile strength varies with test direction approximately in proportion to the ratio of yarn bundle volume. At room temperature the tensile stiffness and strength properties are comparable to the compression properties.
6. The material is rather weak and highly ductile in shear; shear strength is not strongly related to slip plane orientation in the principal directions.
7. There may be a scale effect in strength due to specimen size (the smaller the specimen the greater the strength), but no scale effect was found in modulus.
8. Acoustic emission can be used effectively to distinguish damage sources: low amplitude is identified with matrix crumbling and with shear failures; intermediate amplitude signals are

indicative of fiber crippling and of spalling at the ends of compression specimens; high amplitude signals result from complete, sudden failure of fibers.

9. Cracks appear to originate in matrix pockets, near yarn bundle/matrix pocket interfaces, in a shear mode. The mechanism for this is possibly the stiffness difference between the matrix and the yarn bundle (in the fiber direction), which leads to shear strains in the matrix. Cracks propagate generally in an opening mode configuration, running through large matrix voids, then redirecting along transverse yarn bundle interfaces while shearing easily through bundles in perpendicular directions, then jumping back again to the opening mode configuration.
10. Yarn bundle breaks are rather randomly distributed over a material volume, indicative both of the high nonhomogeneity within the microstructure and of the redundant nature of the material system. Global fracture of the material appears to be a result of the coalescence of numerous small cracks, which link together to form a critical macrocrack.

REFERENCES

- (1) Per telecon between Jon Wilson of FMI and Craig Robinson of SwRI, July 10, 1978.
- (2) Letter from Jon Wilson of FMI to P. H. Francis of SwRI dated September 19, 1977.
- (3) Davidson, D. L., "Fatigue Crack Tip Displacement Observation," Journal of Materials Science, Vol. 14, p. 231, 1979.

FIGURES

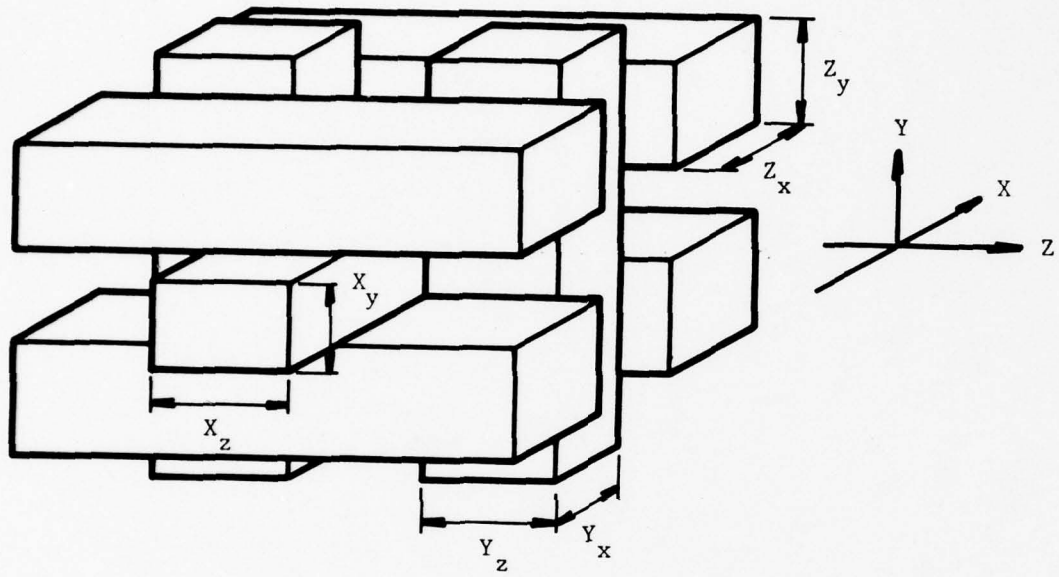


FIGURE 1. BASIC GEOMETRY OF 3-D CARBON-CARBON MATERIAL SYSTEM WITH RECTANGULAR YARN BUNDLES.

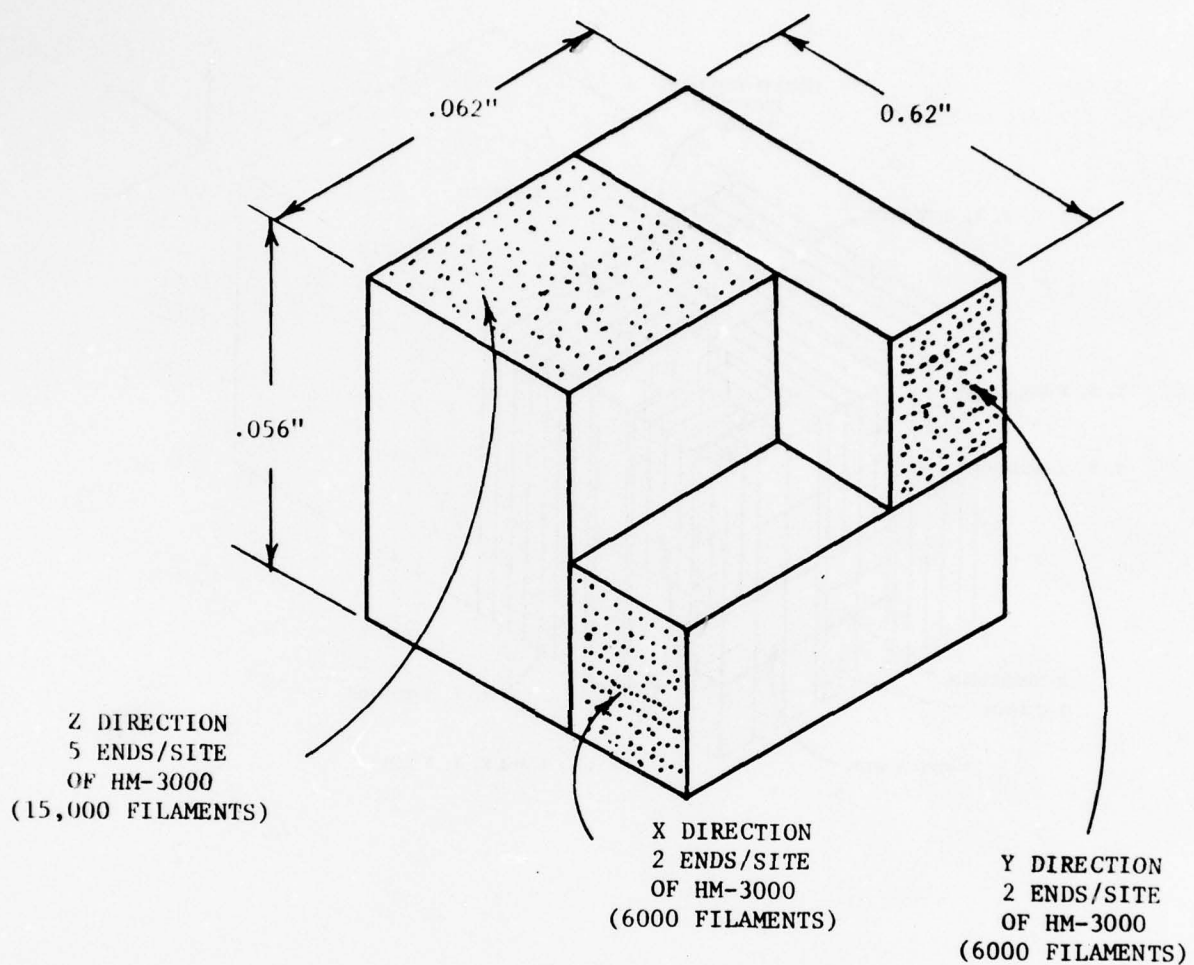


FIGURE 2. SCHEMATIC DRAWING OF UNIT CELL STRUCTURE FOR 2,2,3 CARBON-CARBON MATERIAL. DIMENSIONS FURNISHED BY SUPPLIER (FIBER MATERIAL, INC.).

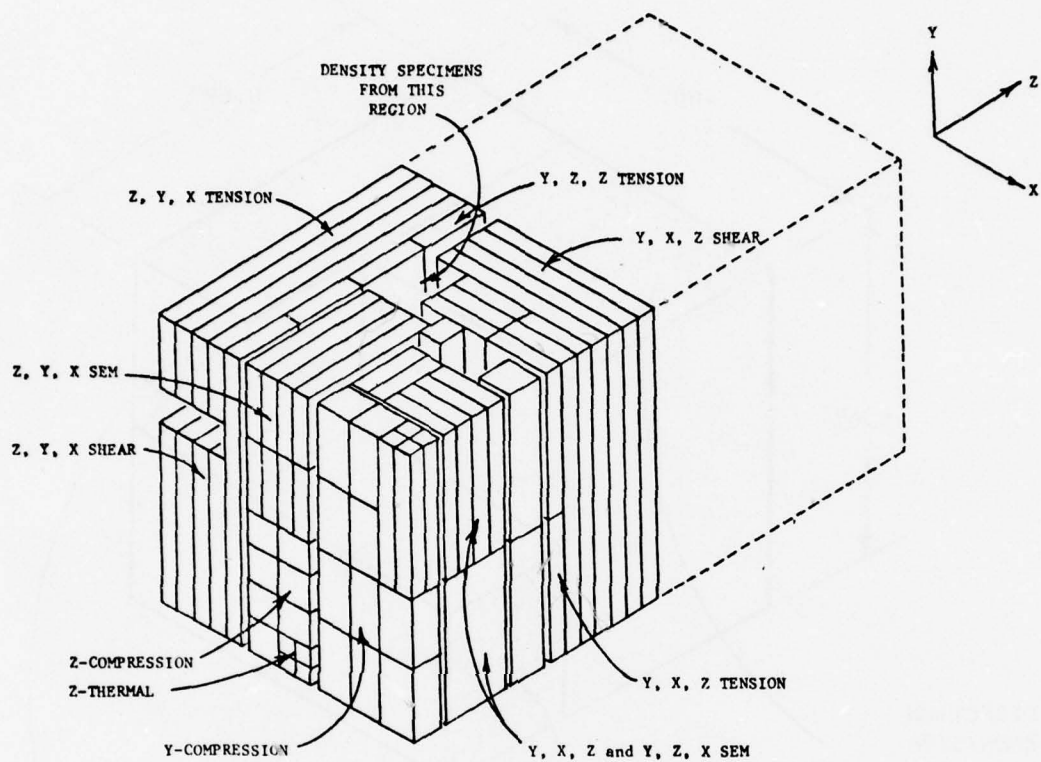


FIGURE 3. CUTTING SCHEME, FOR BILLET NO. 2696, WHICH PRODUCED MECHANICAL TEST SPECIMENS AS WELL AS DENSITY AND THERMAL EXPANSION SPECIMENS.

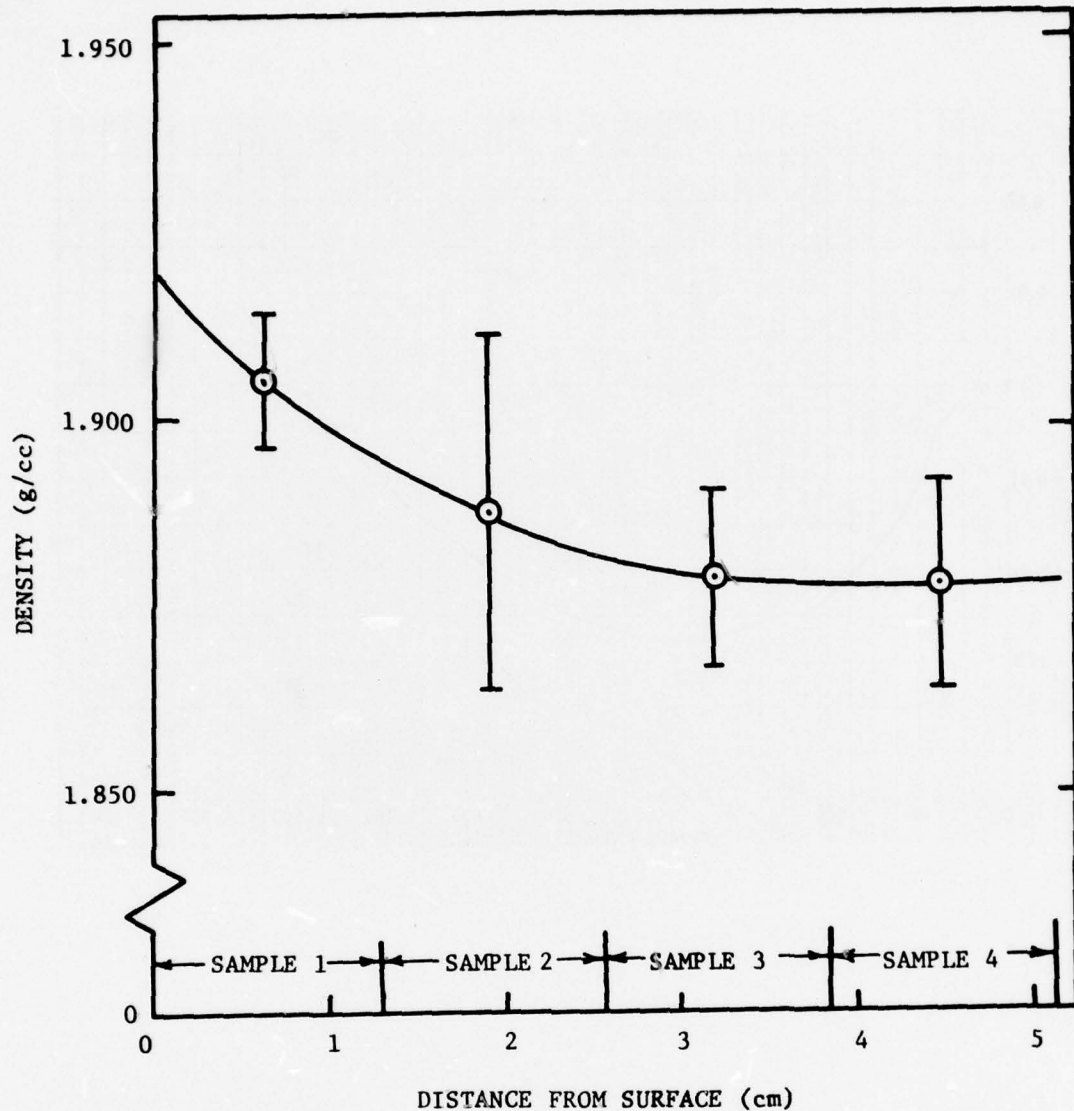


FIGURE 4. DENSITY PROFILE OF AS-RECEIVED CARBON-CARBON BILLET.  
DENSITY SPECIMENS RANGED FROM AN OUTSIDE SURFACE TO  
THE CENTER OF THE BILLET.

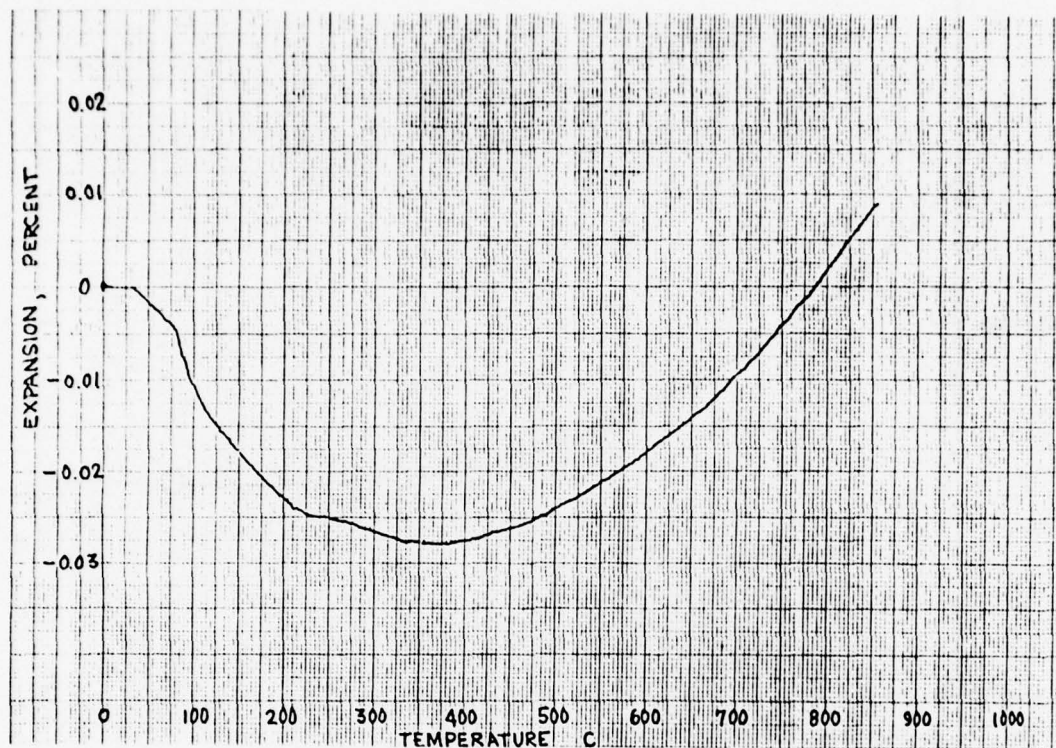


FIGURE 5. TYPICAL THERMAL EXPANSION CURVE FOR THE LOWER TEMPERATURE RANGES AS RECORDED BY A QUARTZ-TUBE DILATOMETER. SPECIMEN NO. TH-1.

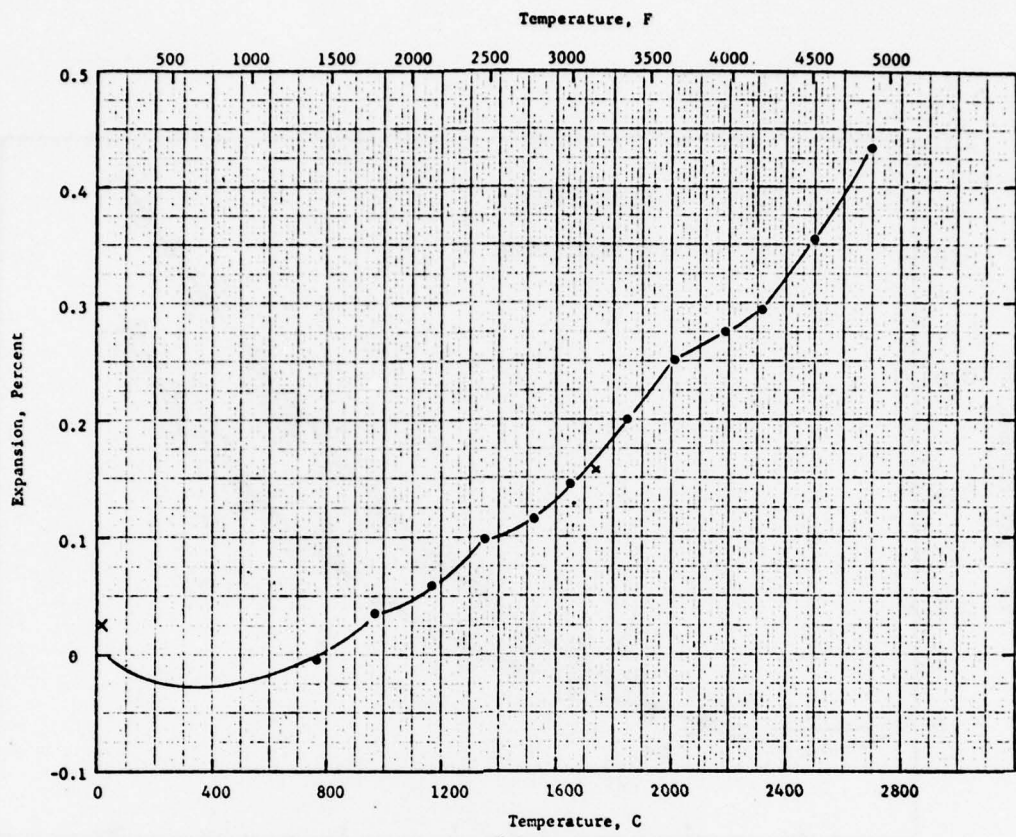


FIGURE 6. TYPICAL THERMAL EXPANSION PROFILE FOR HIGHER TEMPERATURE RANGES AS OBSERVED IN AN OPTICAL DILATOMETER. SPECIMEN TH-1.

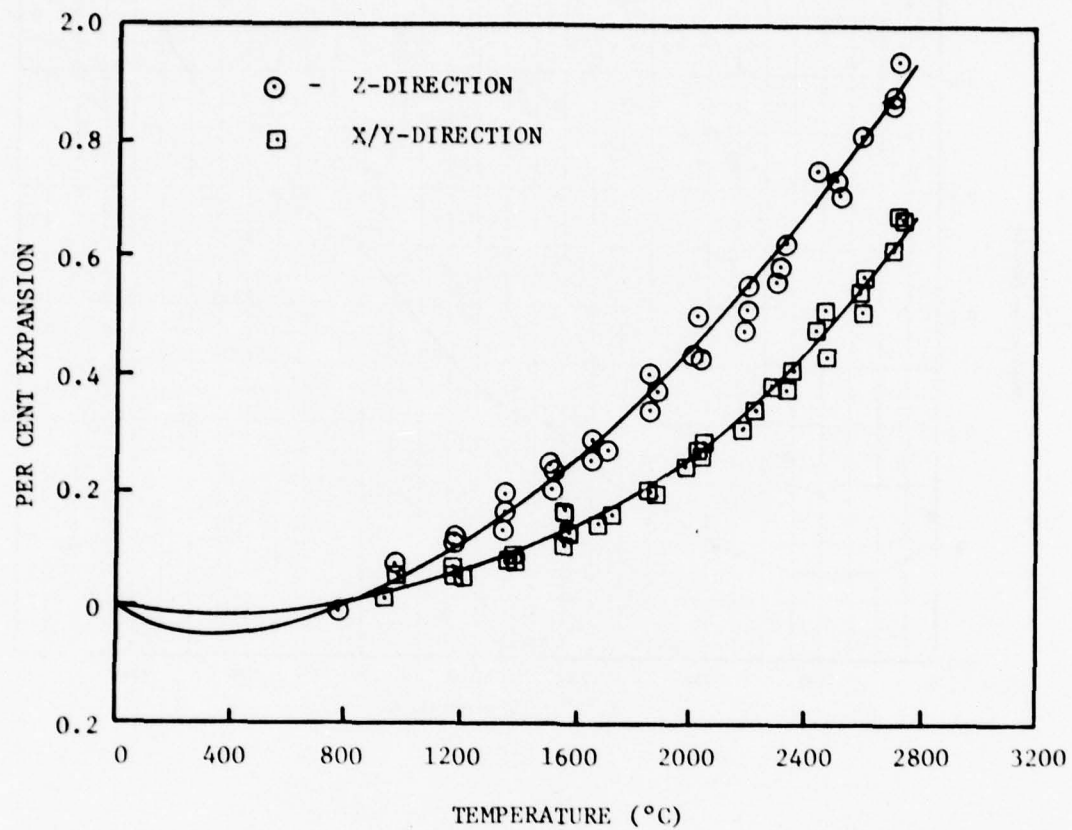


FIGURE 7. COMPLETE THERMAL EXPANSION CURVES FOR BOTH THE Z- AND THE Y-DIRECTIONS, FROM 20°C TO 2700°C.  
THE CURVE SHOWN IS A VISUAL FIT.

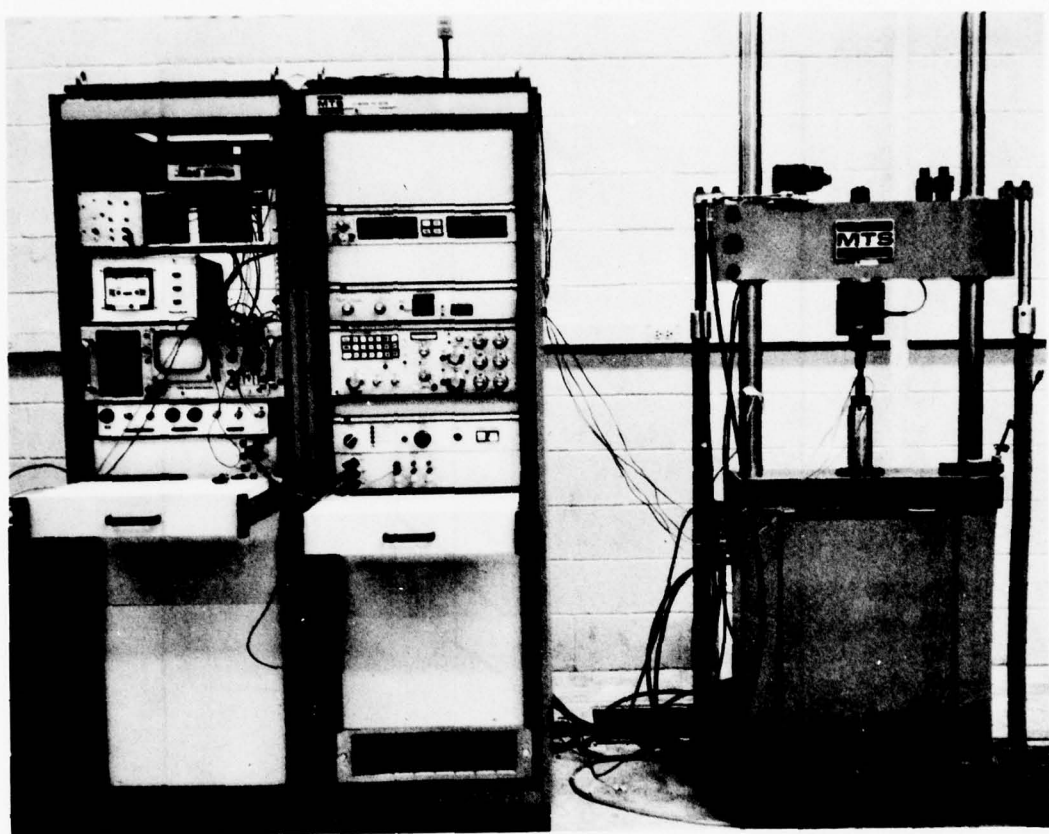


FIGURE 8. MTS MODEL 810 MATERIALS TEST SYSTEM.

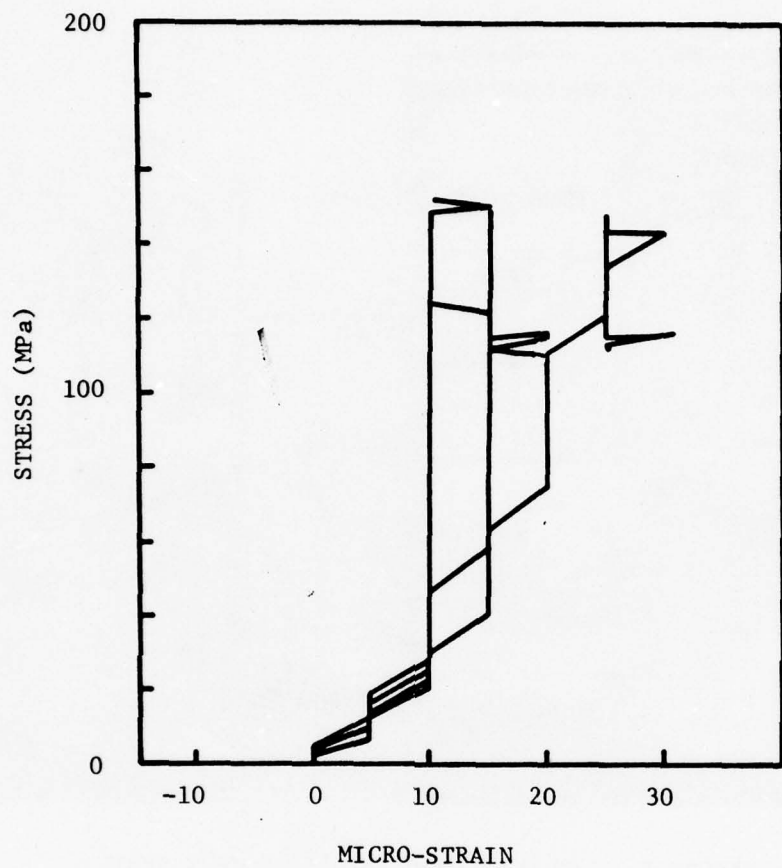


FIGURE 9. TYPICAL STRESS-STRAIN RELATIONS AS MEASURED BY TRANSVERSE STRAIN GAGES ON ALL FOUR SIDES OF A COMPRESSION SPECIMEN. SPECIMEN C-1 (Z-DIRECTION).

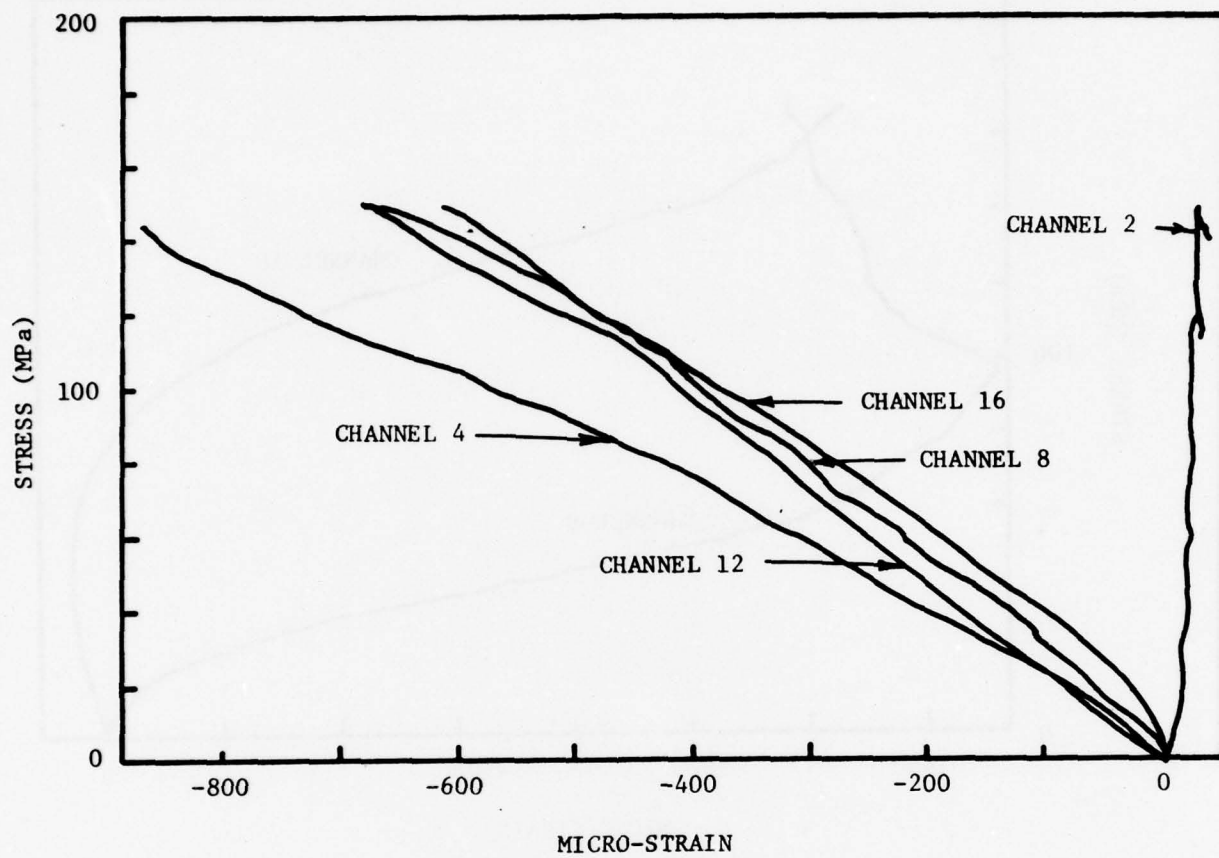


FIGURE 10. TYPICAL STRESS-STRAIN RELATIONS AS MEASURED BY LONGITUDINAL STRAIN GAGES ON ALL FOUR SIDES OF A COMPRESSION SPECIMEN. A TRANSVERSE CHANNEL IS SHOWN FOR COMPARISON. SPECIMEN C-1 (Z-DIRECTION).

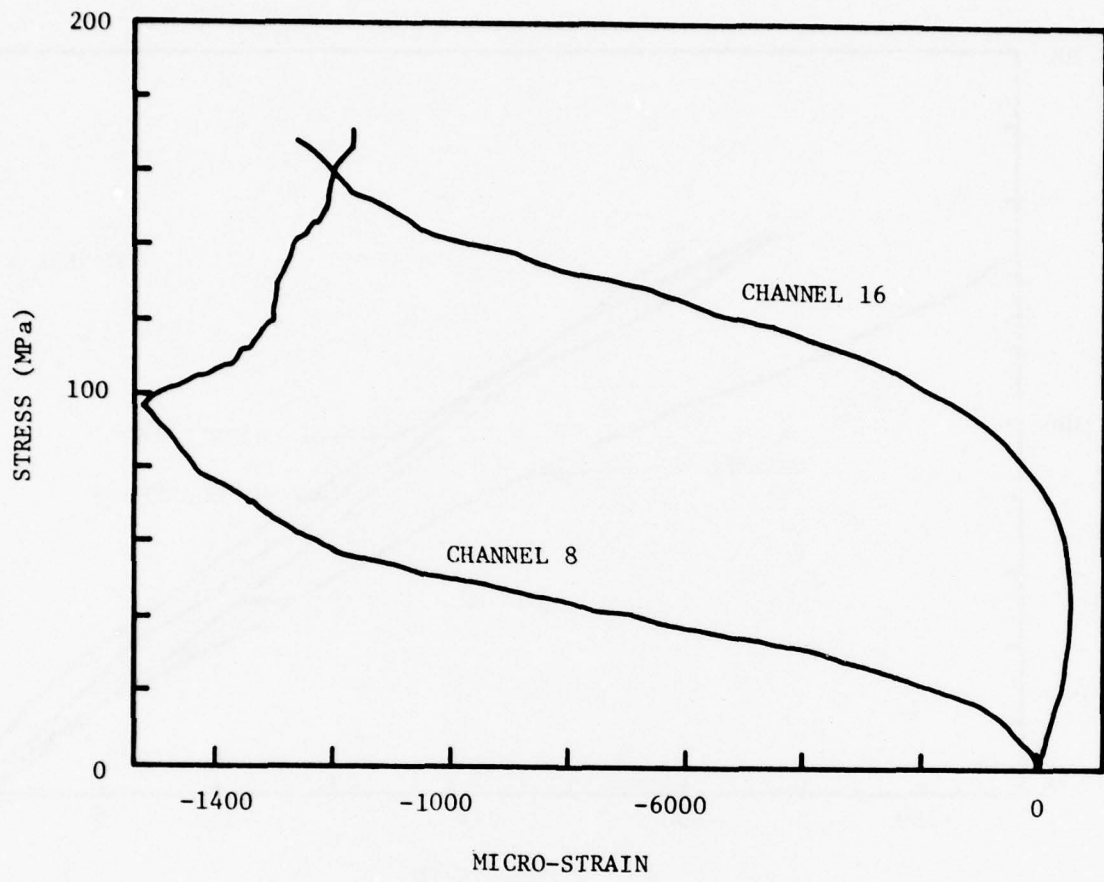


FIGURE 11. STRESS-STRAIN RELATIONS FOR TWO GAGES  
ON OPPOSITE SIDES OF A SPECIMEN WHICH  
EXHIBITED CONSIDERABLE BENDING DURING  
A COMPRESSION TEST. SPECIMEN C-3  
(Z-DIRECTION).

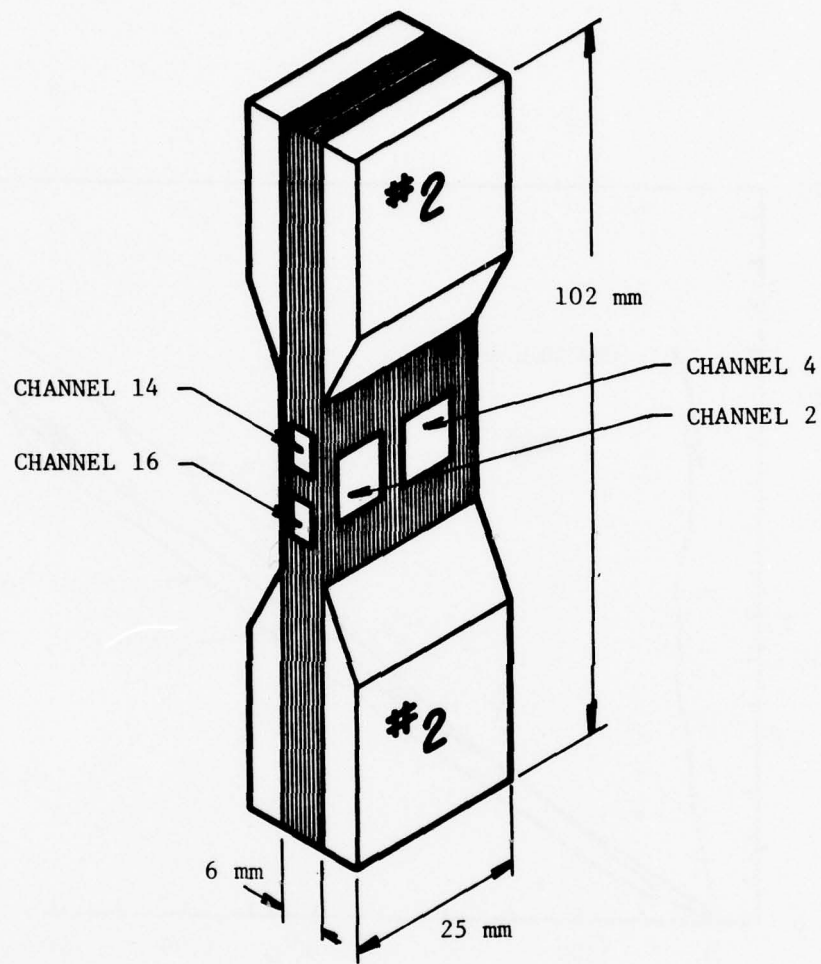


FIGURE 12. SKETCH OF TYPICAL TENSION SPECIMEN  
WITH BIAXIAL STRAIN GAGES ON EACH  
FACE.

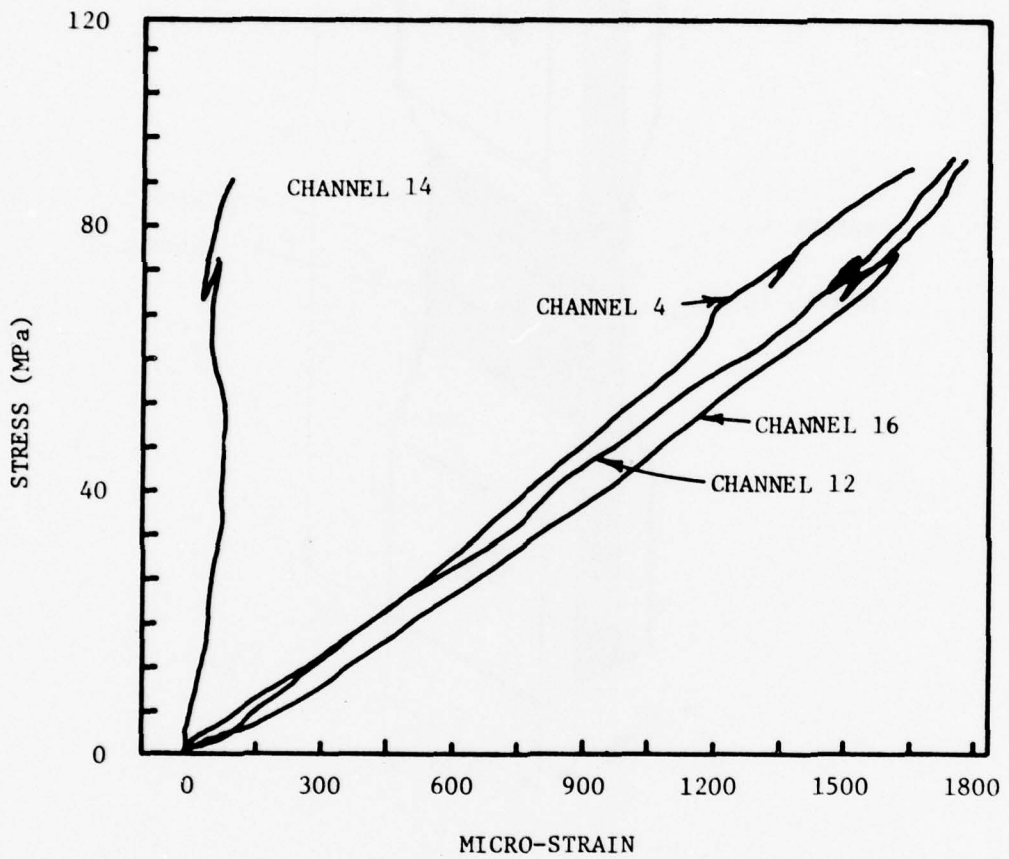


FIGURE 13. TYPICAL STRESS-STRAIN RELATIONS FOR THREE LONGITUDINAL STRAIN GAGES (THE FOURTH GAGE SHORTED OUT) ON A TENSILE SPECIMEN. A STRAIN READING FROM A TRANSVERSE GAGE IS SHOWN FOR COMPARISON (CHANNEL 14). SPECIMEN T-7 (Y-DIRECTION).

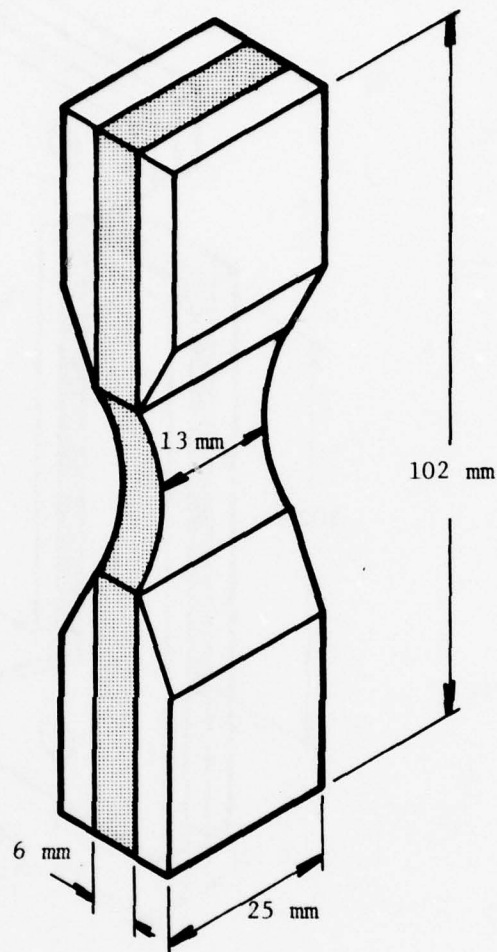


FIGURE 14. SKETCH OF TENSILE SPECIMEN WITH A  
REDUCED CROSS-SECTIONAL AREA IN  
THE CRITICAL TEST REGION.

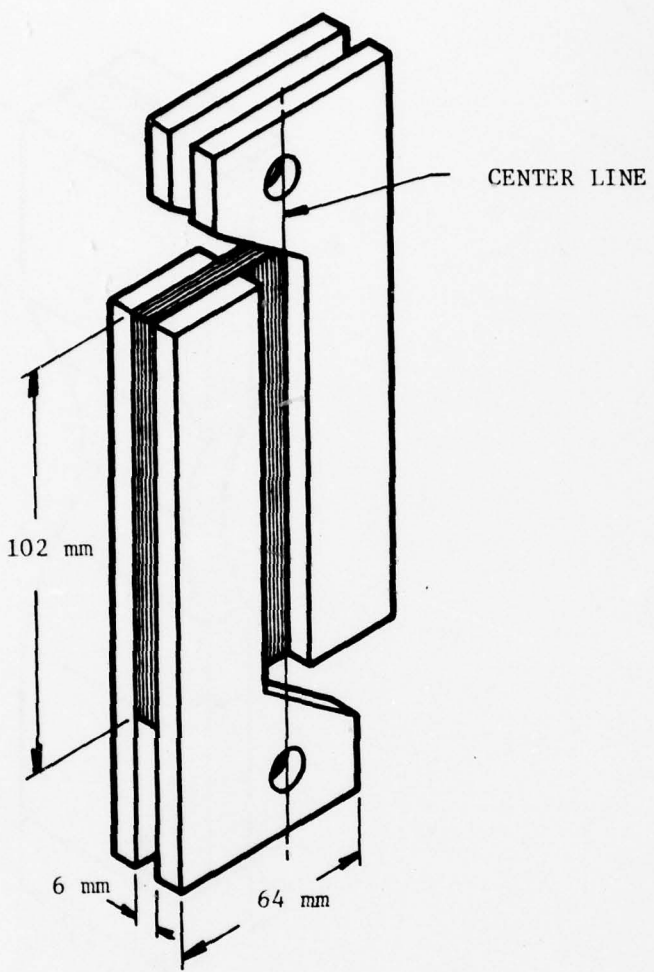


FIGURE 15. SCHEMATIC DRAWING OF RAIL SHEAR SPECIMEN.

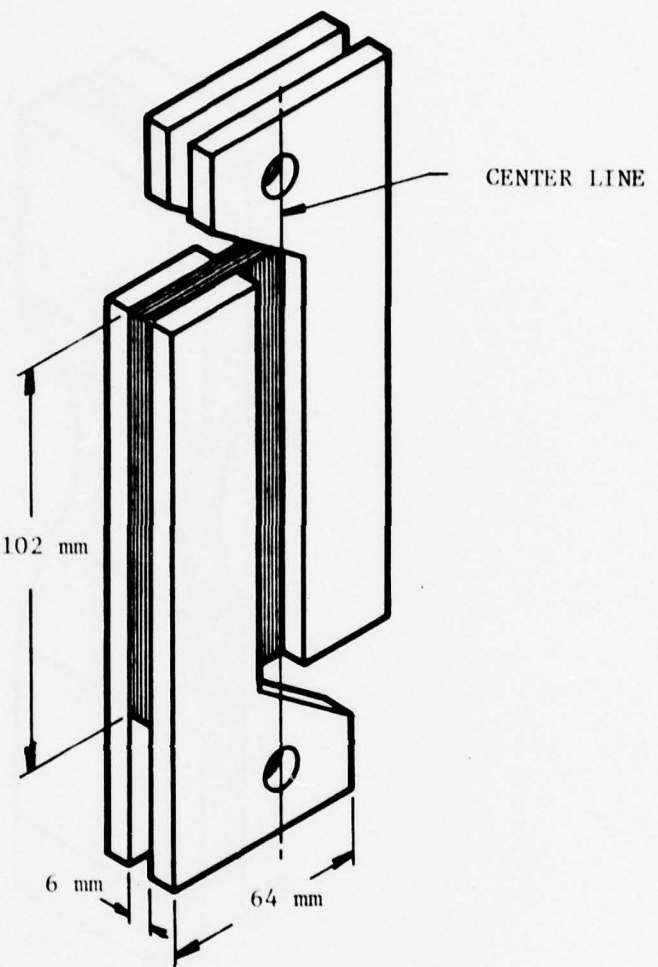


FIGURE 15. SCHEMATIC DRAWING OF RAIL SHEAR SPECIMEN.

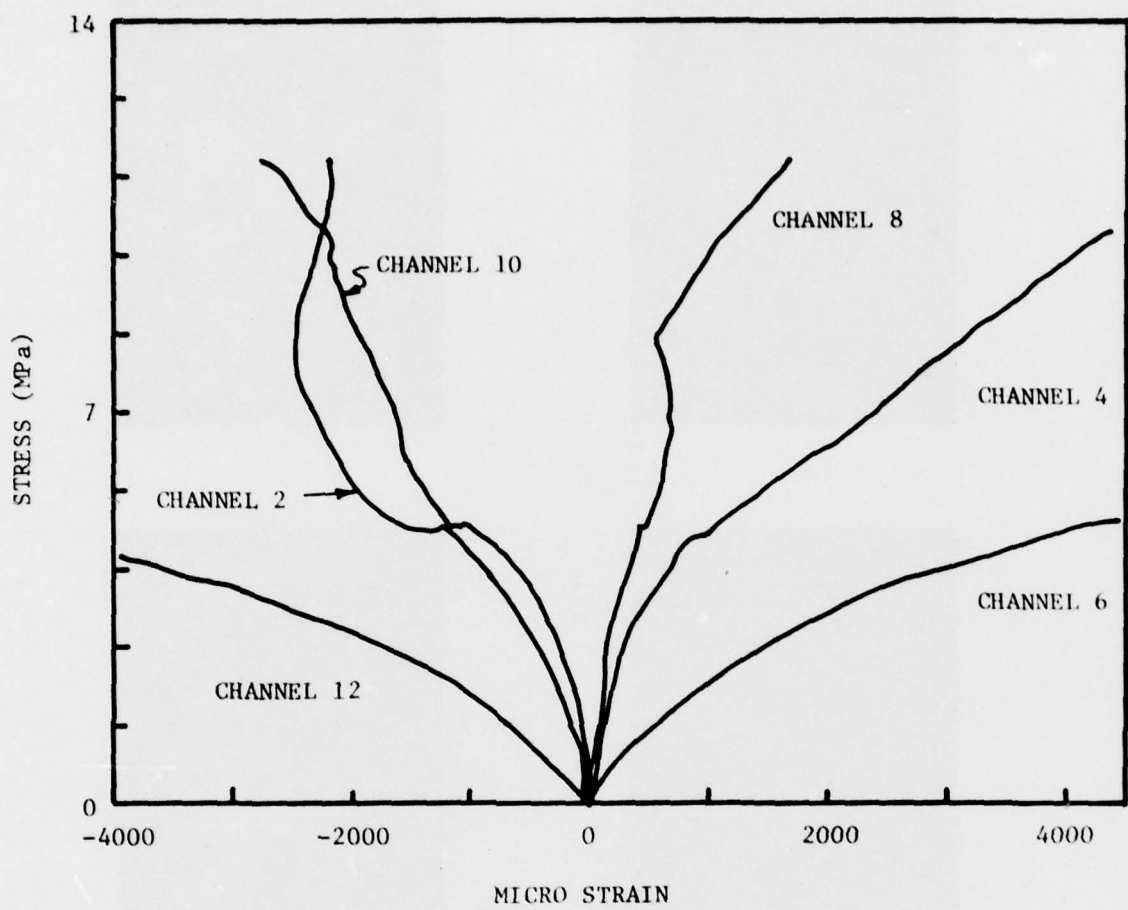
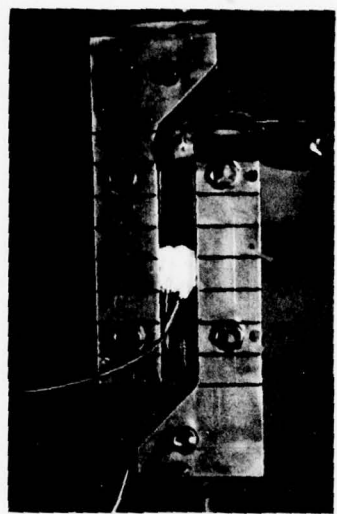
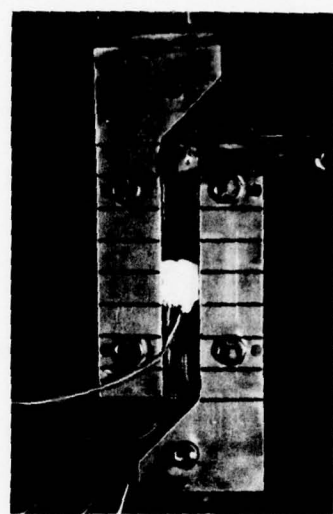


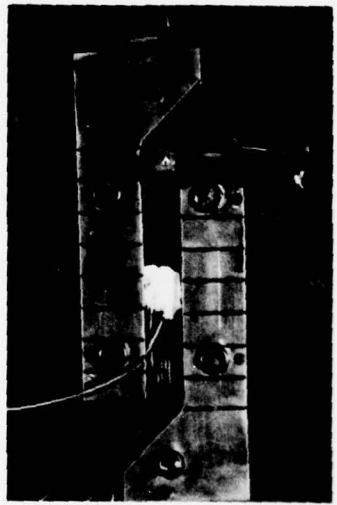
FIGURE 16. TYPICAL STRESS-STRAIN CURVES FOR RAIL SHEAR TESTS. SPECIMEN S-6 (Y-DIRECTION) CHANNELS 2 AND 8 ARE STRAINS PERPENDICULAR; CHANNELS 4 AND 10 ARE PARALLEL; AND CHANNELS 6 AND 12 ARE ORIENTED AT  $45^\circ$  TO THE LOADING DIRECTION.



(a)



(b)



(c)



(d)

FIGURE 17. LOADING SEQUENCE DURING RAIL SHEAR TEST.  
SPECIMEN S-2: 00 MPa, 6.4 MPa (0.93 ksi),  
14.4 MPa (2.09 ksi), 17.2 MPa (2.50 ksi).  
ACOUSTIC EMISSION TRANSDUCER IS ATTACHED  
TO THE TOP REGION OF THE SPECIMEN IN a,  
b and c.

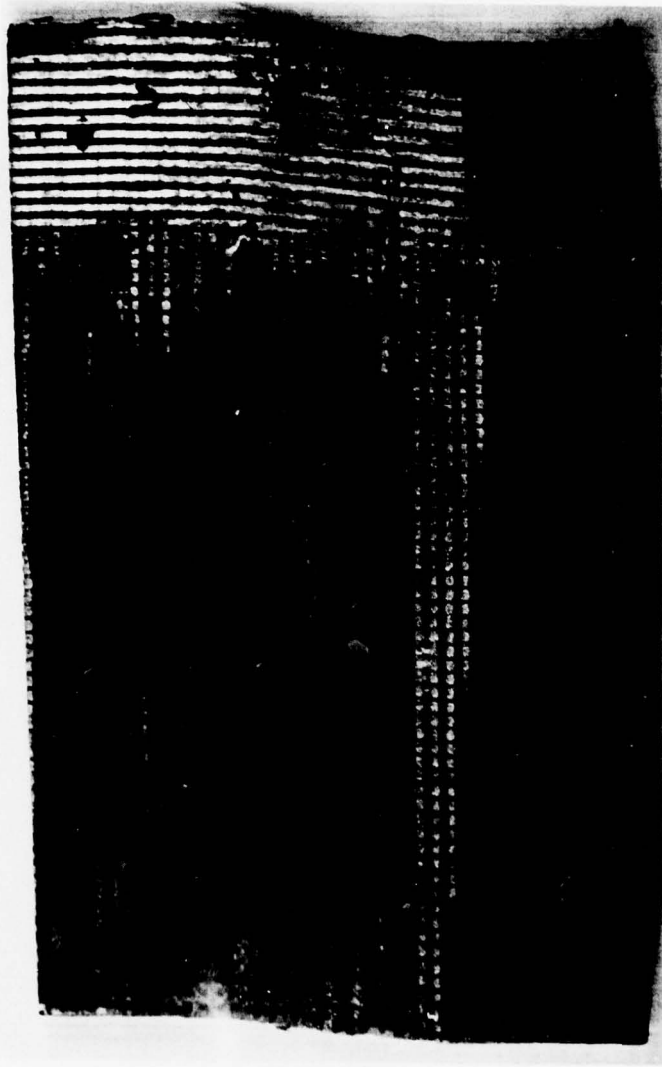
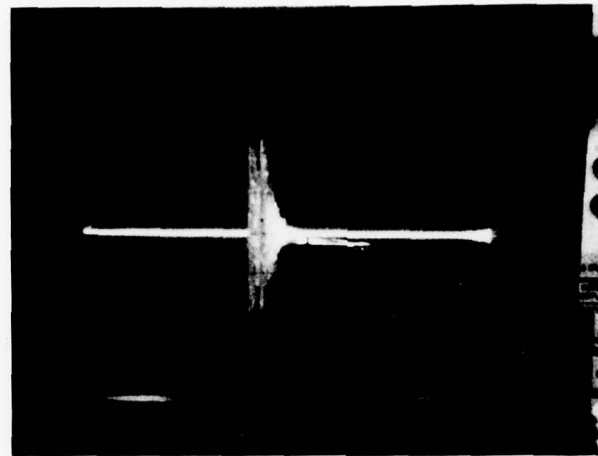


FIGURE 18. SHEAR SPECIMEN AFTER TEST WAS RUN. NOTE SUBSTANTIAL AMOUNT OF PLASTIC DEFORMATION WHICH SPECIMEN SUSTAINED WITHOUT CATASTROPHIC FAILURE.

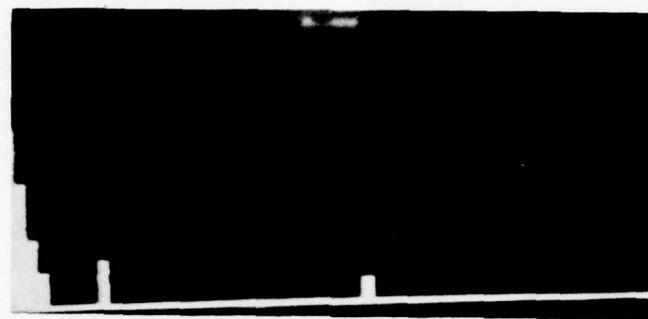


(a)

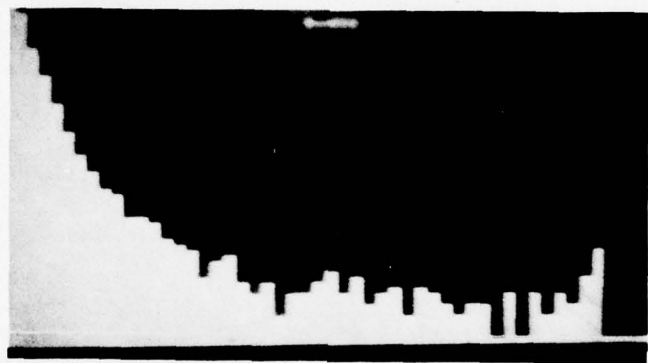


(b)

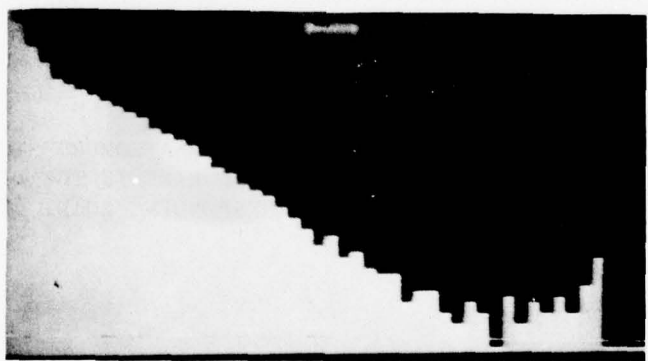
FIGURE 19. PENTEL 0.5mm LEAD BREAK ON SPECIMEN C-24:  
a) 0.2 VOLTS PER DIVISION - VERTICAL;  
1 MILLISECOND PER DIVISION - HORIZONTAL,  
150-400 KHz BANDPASS; 40 dB GAIN; b) COUNT  
DISTRIBUTION GRAPH; 60 dB GAIN.



(a)



(b)



(c)

FIGURE 20. COUNT DISTRIBUTION GRAPH, SPECIMEN C-10;  
40 dB GAIN: a) 46 MPa (6.67 ksi);  
b) 75 MPa (10.8 ksi); c) END OF TEST.

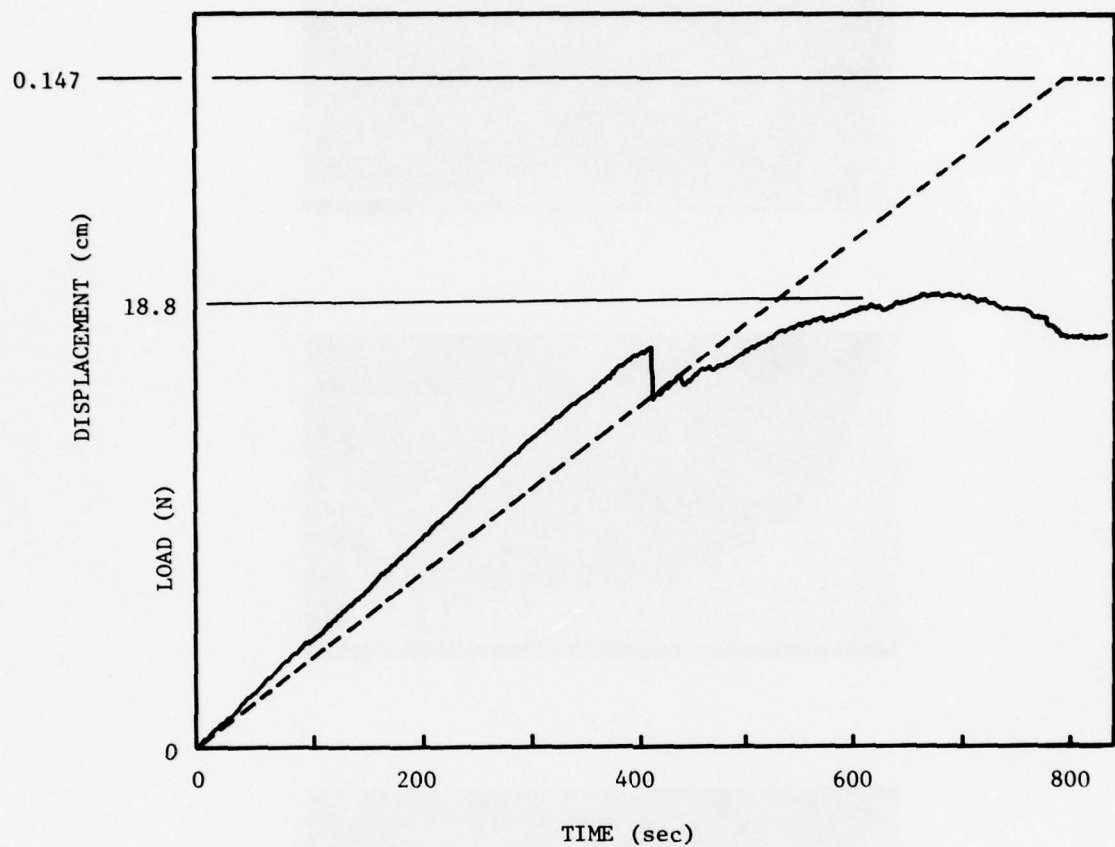
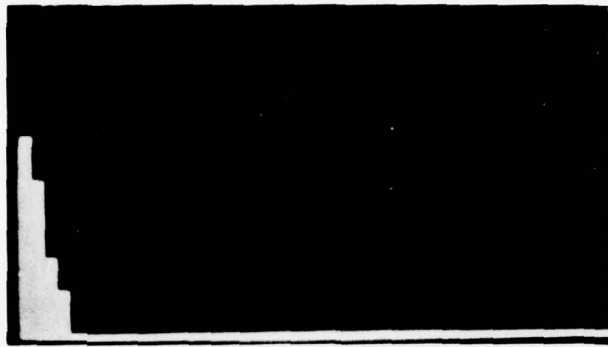
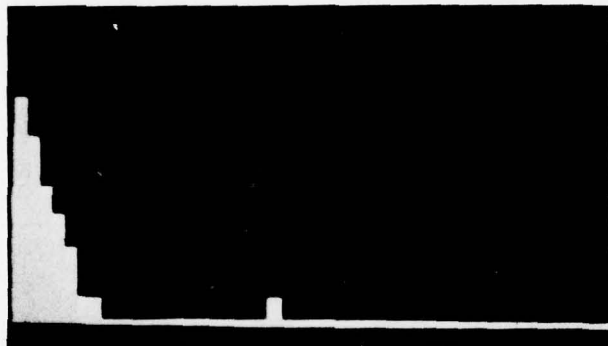


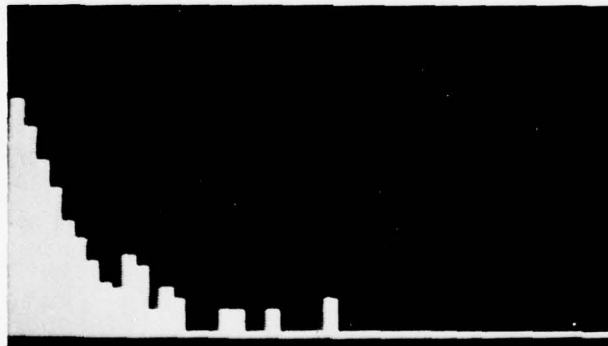
FIGURE 21. TYPICAL LOAD-DISPLACEMENT CURVE FOR A COMPRESSION TEST UNDER DISPLACEMENT CONTROL. THE BROKEN LINE IS THE DISPLACEMENT AND THE SOLID LINE IS THE CORRESPONDING LOAD. SPECIMEN C-19.



(a)



(b)



(c)

FIGURE 22. AE COUNT DISTRIBUTION GRAPH FOR  
SPECIMEN T-3. 40 dB GAIN: a)  
53 MPa (7.8 ksi); b) 80 MPa  
(11.6 ksi); c) 138 MPa (19.4 ksi),  
END OF TEST.

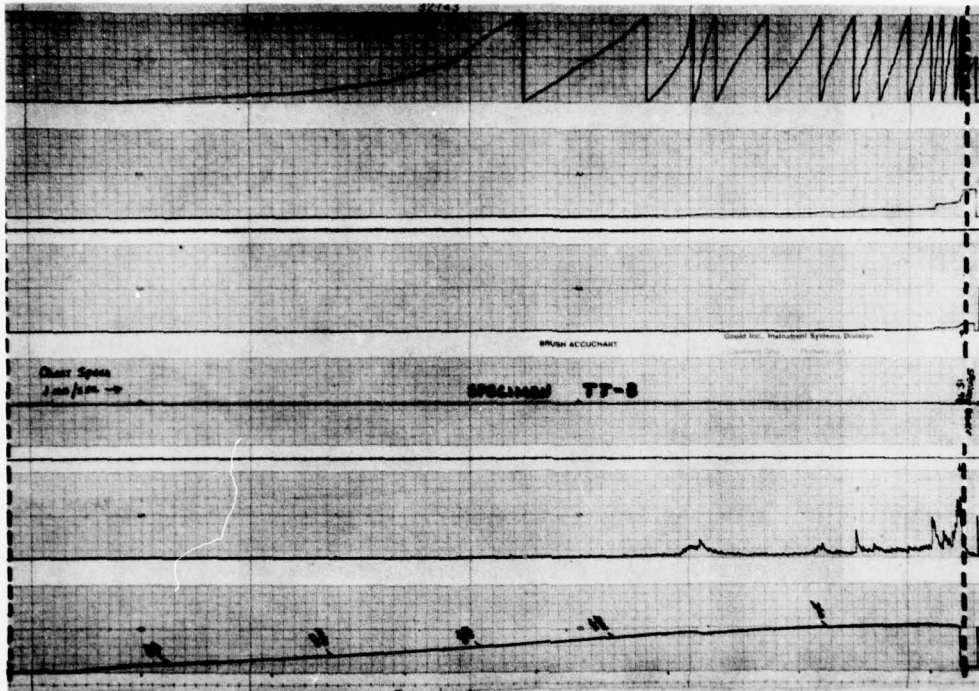


FIGURE 23. ACOUSTIC EMISSION DATA. BOTTOM CHANNEL IS LOAD, 5000 POUND, FULL-SCALE. SECOND CHANNEL IS COUNT RATE WITH 10 mV THRESHOLD; FULL SCALE IS 5V. CHANNELS 4-6 ARE ACCUMULATED RING-DOWN COUNTS WITH THRESHOLDS OF 400 mV, 100 mV AND 10 mV, RESPECTIVELY; FULL SCALE IS 65,536 COUNTS. (SPECIMEN TT-3)

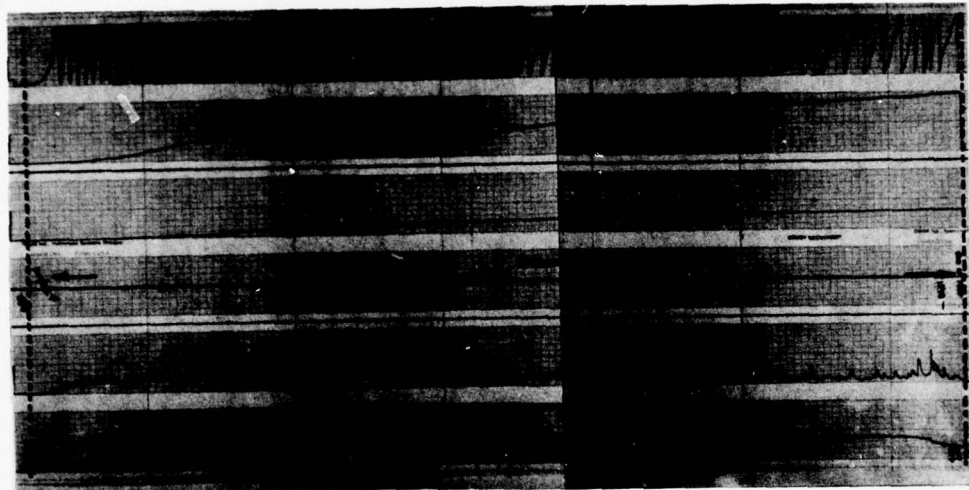


FIGURE 24. FIVE CHANNEL RECORDING OF AE DATA  
(SEE FIGURE 23 FOR DETAILS) FOR  
SHEAR SPECIMEN (#S-7).

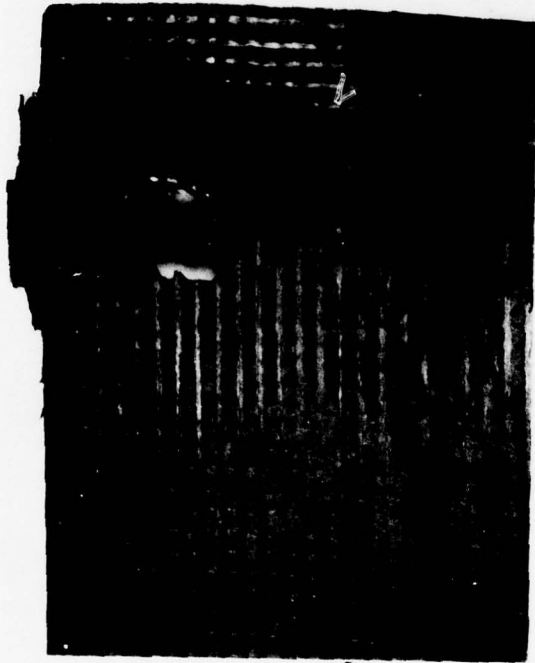


FIGURE 25. TYPICAL PHENOMENON SEEN IN SHEAR SPECIMENS (SPECIMEN S-7). PIN HOLES WERE USED TO PUT PRESSURE AGAINST SHEAR GRIPS IN ORDER TO ACHIEVE BETTER ADHESION WITH SPECIMENS.

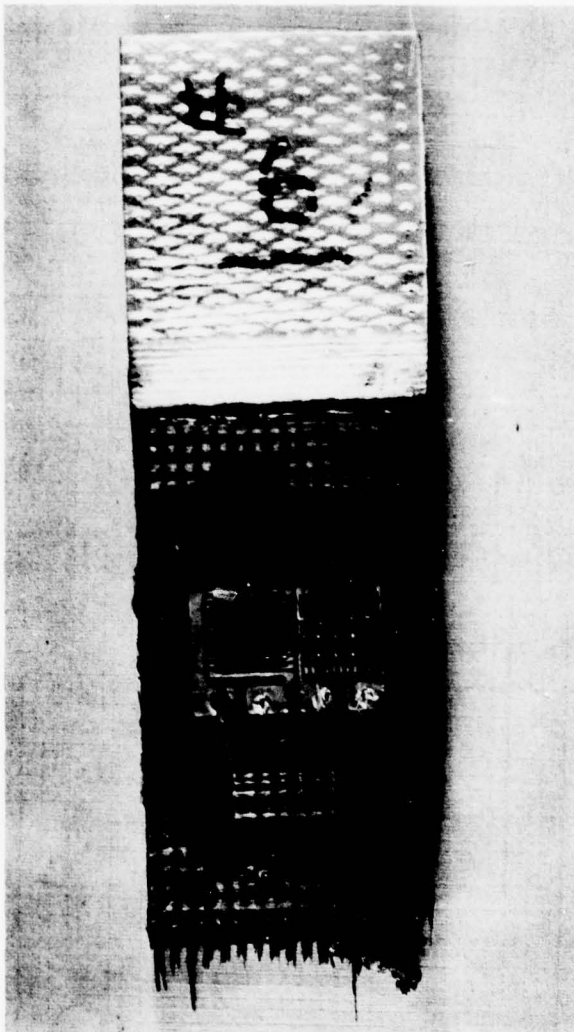


FIGURE 26. FAILED TENSILE SPECIMEN (SPECIMEN T-6) SHOWING VERY LOCALIZED FIBER FRACTURE. ORIENTATION OF THE SPECIMEN IS Y, Z, X (Y-BUNDLES ALONG THE LENGTH, TENSILE AXIS; Z-BUNDLES ACROSS THE WIDTH; AND X-FIBER BUNDLES THROUGH THE THICKNESS).

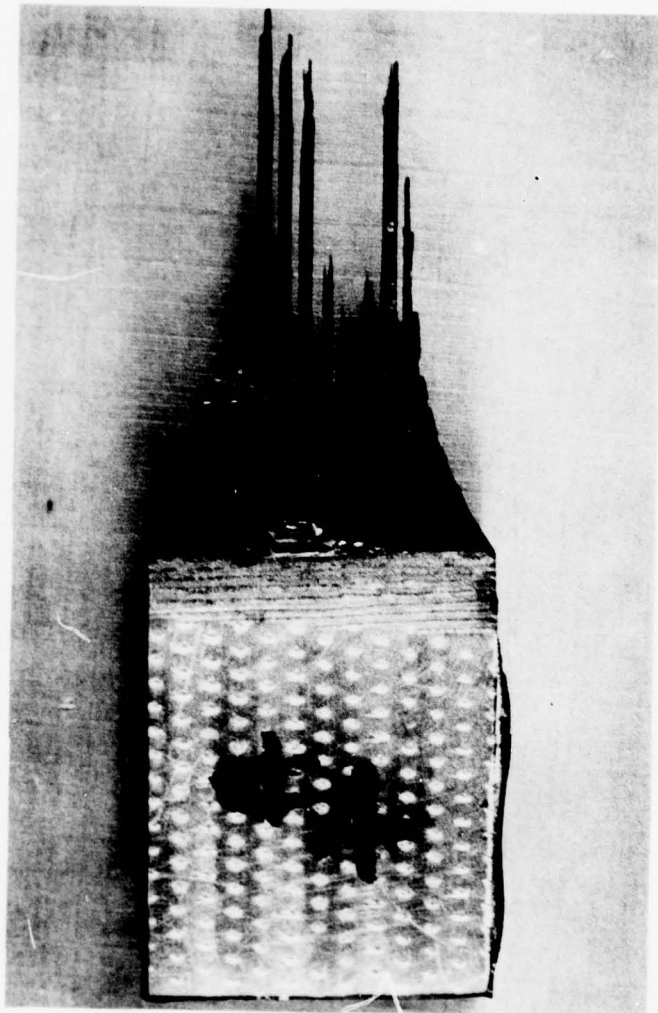


FIGURE 27. FAILED TENSILE SPECIMEN (T-4) SHOWING RANDOM FIBER FAILURE LOCATION. ORIENTATION OF SPECIMEN IS Z, Y, X.

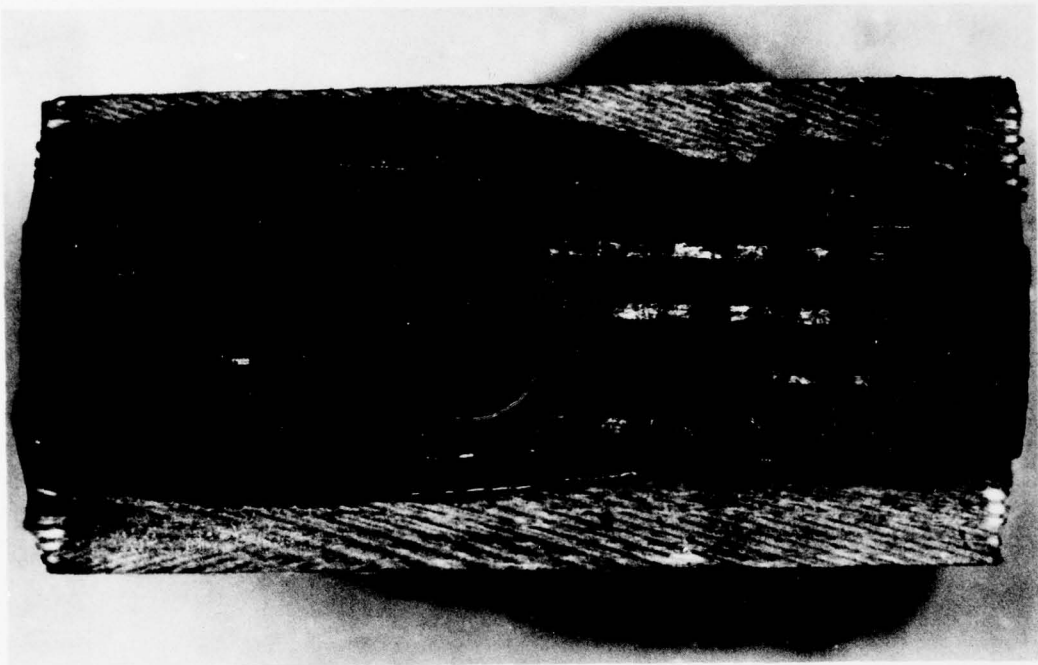


FIGURE 28. FAILED TENSILE SPECIMEN (SPECIMEN T-4) SHOWING LONGITUDINAL FIBERS WHICH HAVE PULLED OUT OF SURROUNDING MATRIX AND TRANSVERSE FIBER BUNDLE REGIONS, AT THE END OF THE SPECIMEN. SPECIMEN IS FOUR UNIT CELLS THICK.

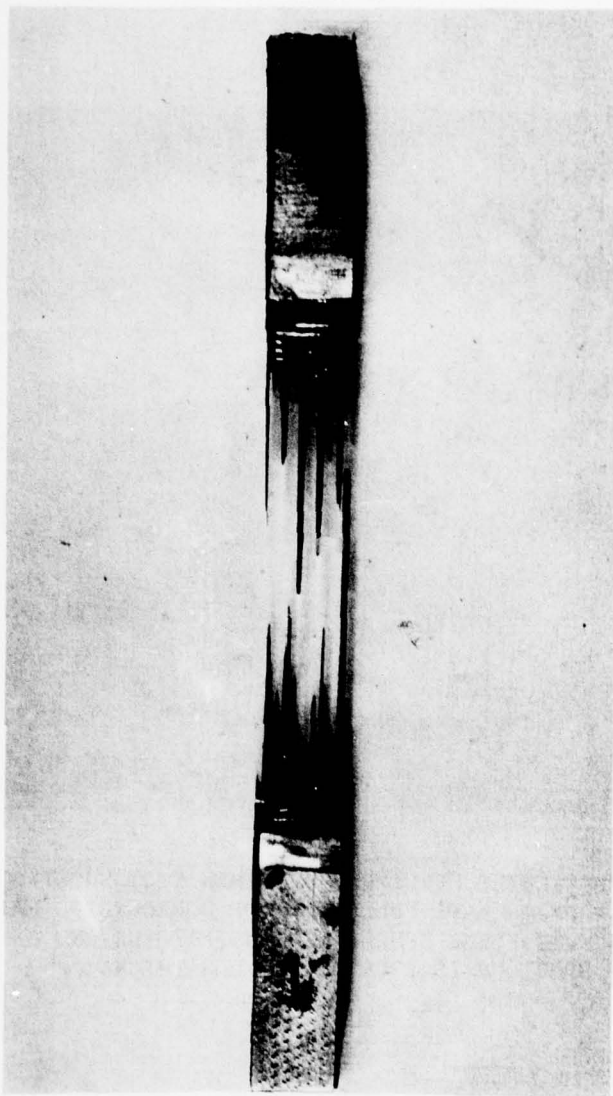


FIGURE 29. FAILED TENSILE SPECIMEN (SPECIMEN TT-1)  
SHOWING SOME FIBERS WHICH PULLED COMPLETELY OUT OF THE SURROUNDING STRUCTURE.  
SPECIMEN IS TWO UNIT CELLS THICK.

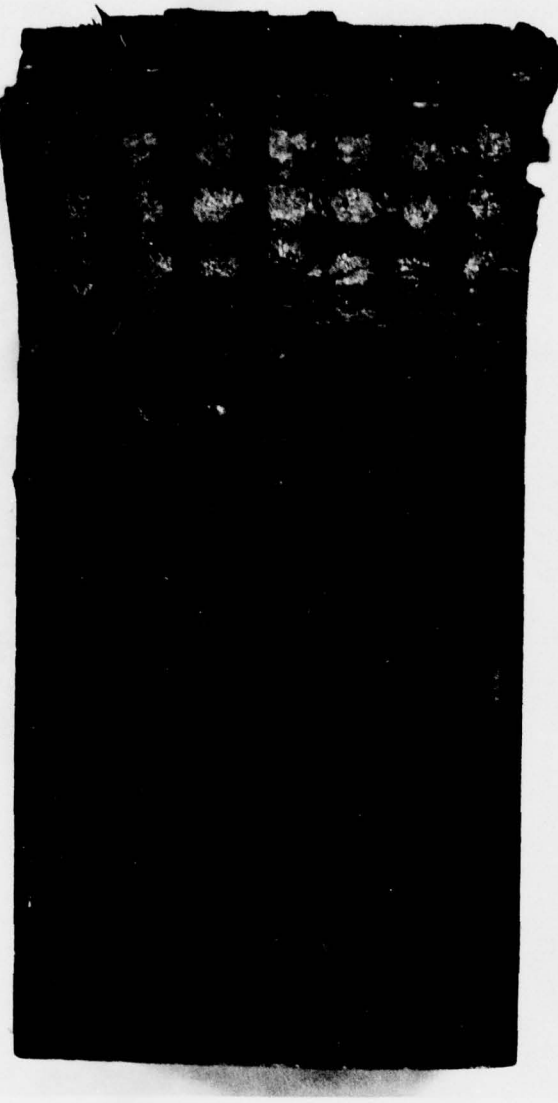


FIGURE 30. FAILED COMPRESSION SPECIMEN (SPECIMEN C-24)  
SHOWING BROOMING PHENOMENON.

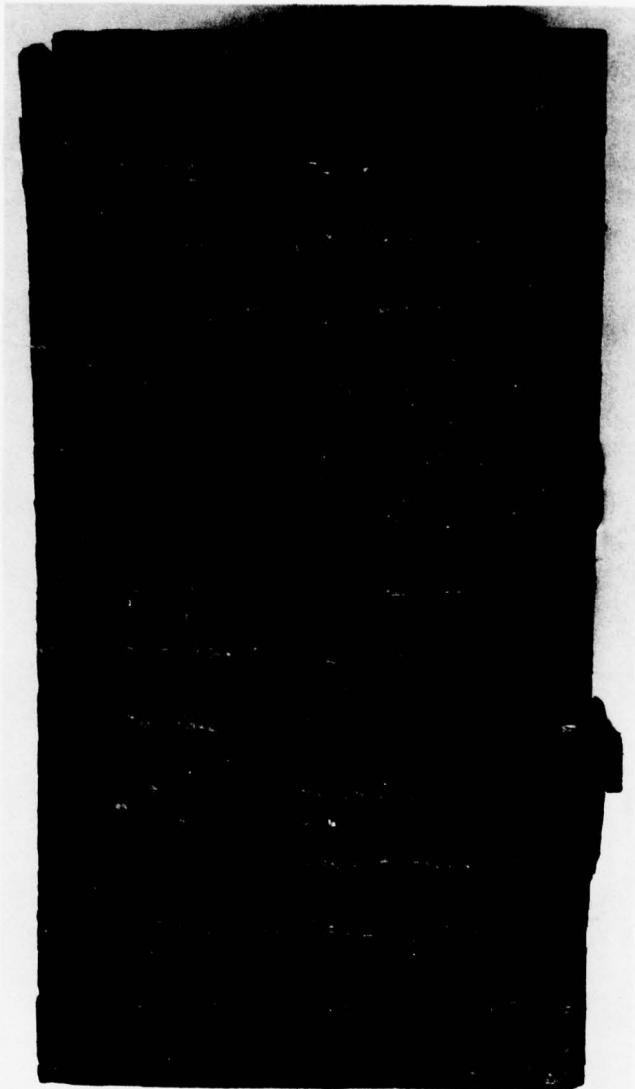


FIGURE 31. FAILED COMPRESSION SPECIMEN (SPECIMEN C-19)  
SHOWING NORMAL DISPLACEMENT OF TRANSVERSE  
FIBER BUNDLES.

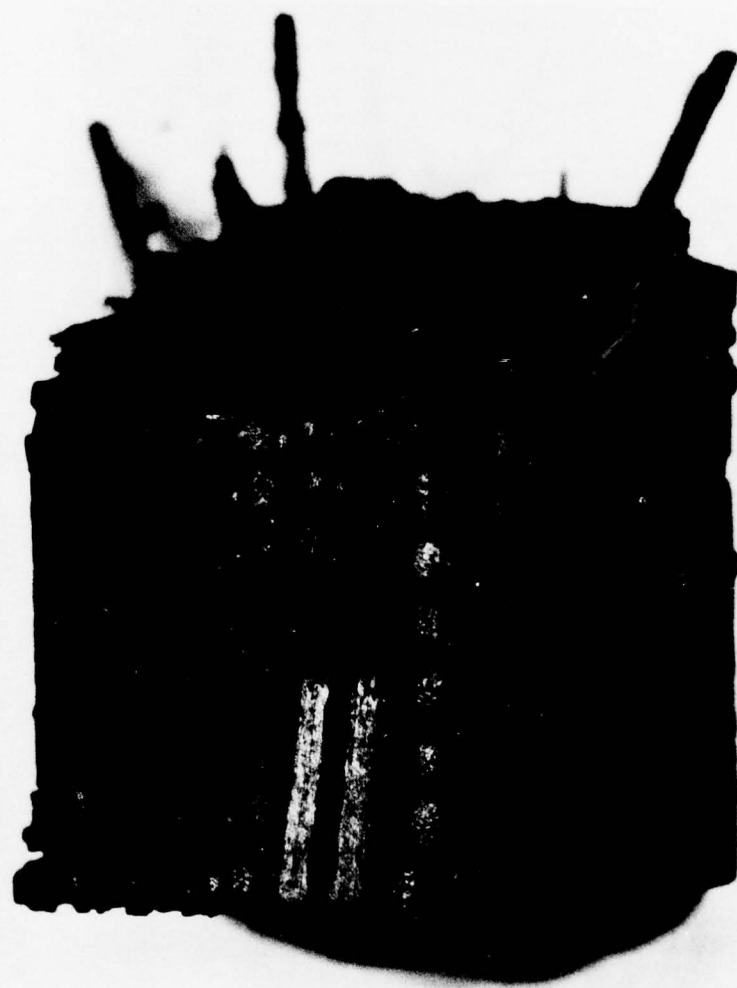


FIGURE 32. FAILED COMPRESSION SPECIMEN (SPECIMEN C-20, Y-DIRECTION) SHOWING SHEAR-LIKE FAILURE SURFACE. FAILURE PLANE IS AT AN ANGLE OF 25° TO 30° FROM PLANE NORMAL TO LOADING DIRECTION. TEST TEMPERATURE WAS 1370°C (2500°F).



FIGURE 33. FAILED COMPRESSION SPECIMEN (SPECIMEN C-11,  
Z-DIRECTION) SHOWING SHEAR-LIKE FAILURE.  
TEST TEMPERATURE WAS 1930°C (3500°F).

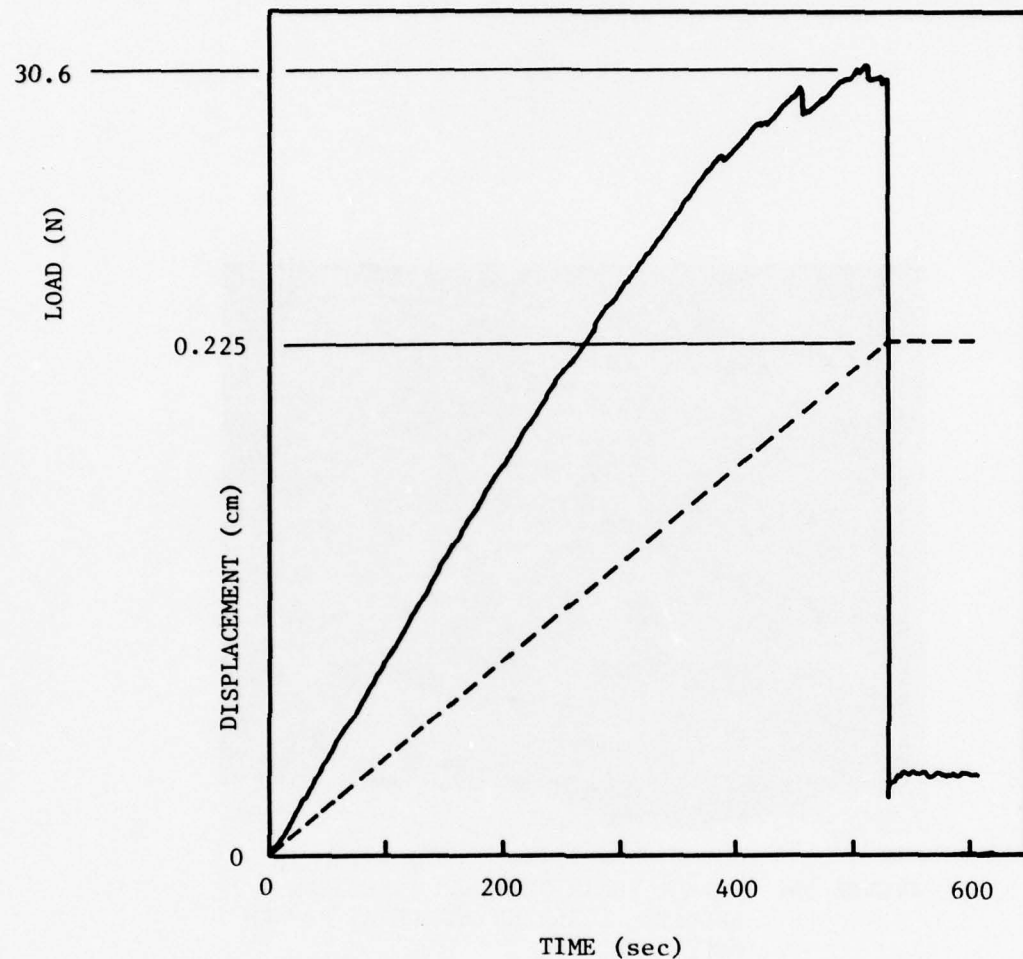


FIGURE 34. LOAD VERSUS DISPLACEMENT CURVE FOR HIGH TEMPERATURE ( $1930^{\circ}\text{C}$ ,  $3500^{\circ}\text{F}$ ) COMPRESSION TEST, SHOWING SUDDEN, CATASTROPHIC FAILURE. THE BROKEN LINE IS DISPLACEMENT AND THE SOLID LINE IS THE CORRESPONDING LOAD. (SPECIMEN C-11, Z-DIRECTION).

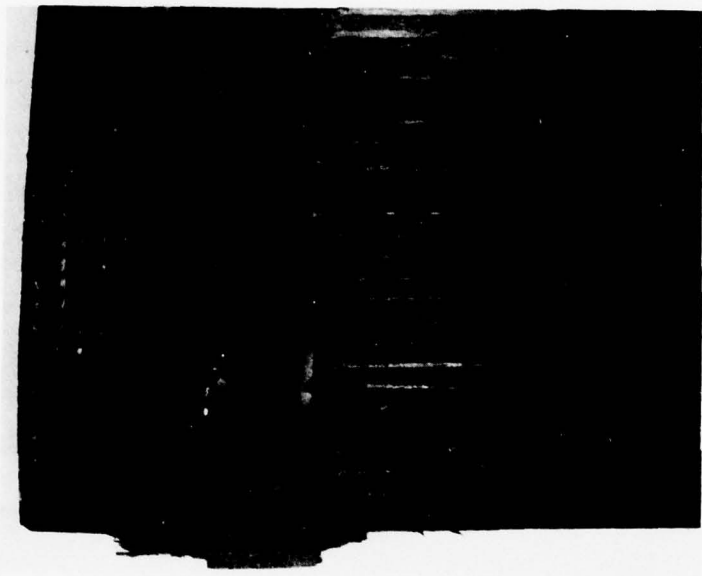


FIGURE 35. FAILED SHEAR SPECIMEN (SPECIMEN S-2)  
SHOWING LOCALIZED DAMAGE AT PINNED  
HOLE.

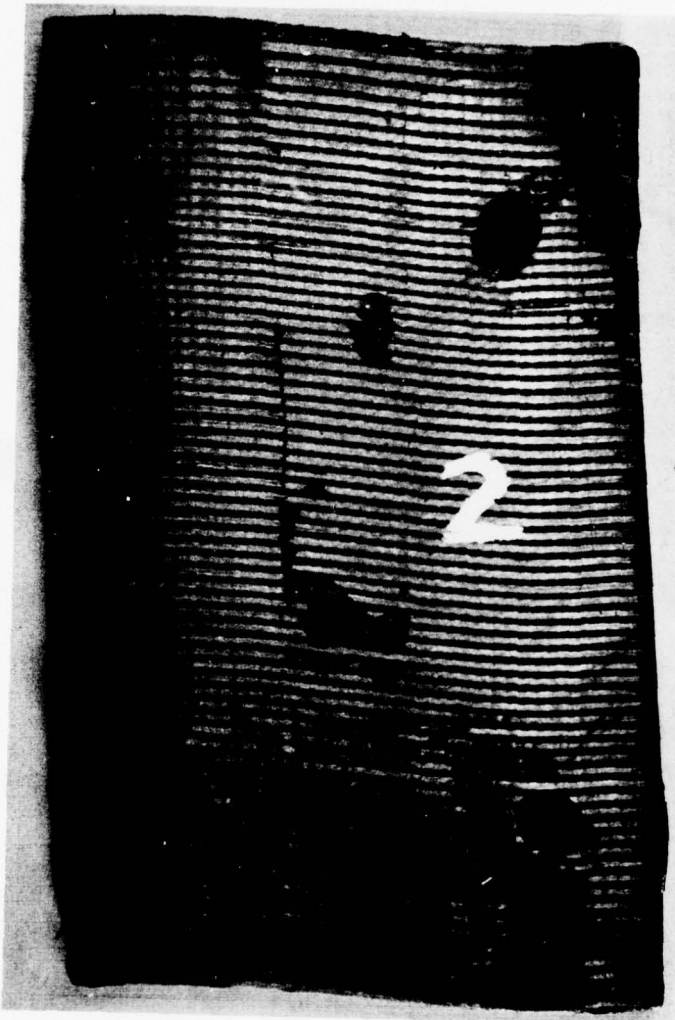


FIGURE 36. FAILED SHEAR SPECIMEN (SPECIMEN S-2)  
SHOWING LARGE AMOUNT OF PLASTIC  
DEFORMATION.

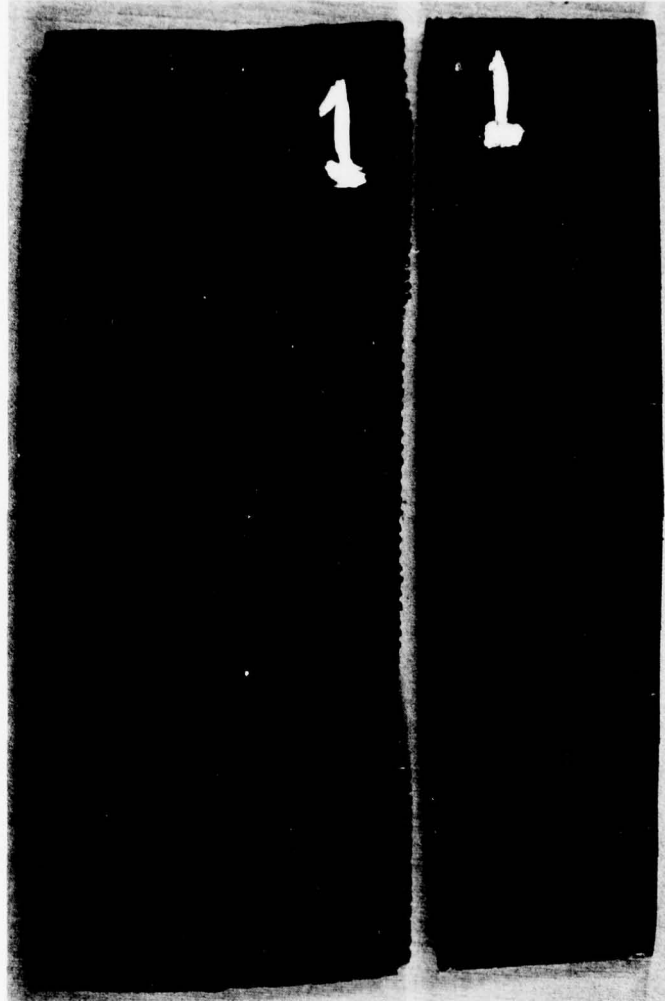


FIGURE 37. FAILED SHEAR SPECIMEN (SPECIMEN S-1)  
SHOWING UNUSUAL PHENOMENON OF  
"BRITTLE" FAILURE.

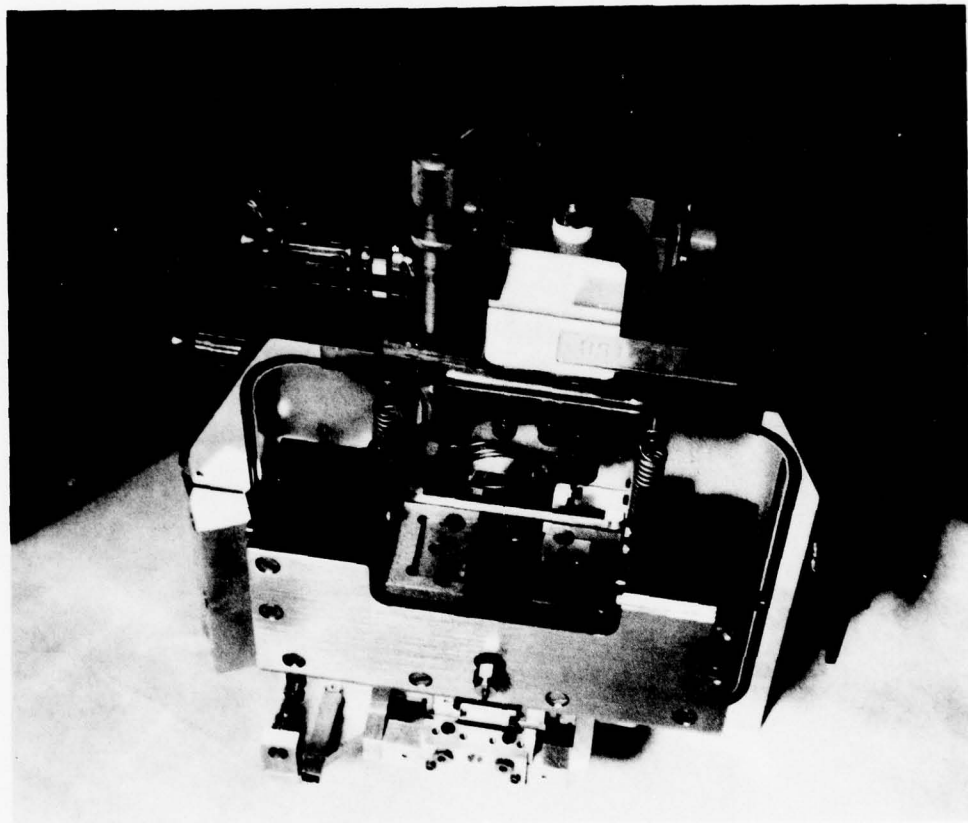


FIGURE 38. LOADING STAGE FOR ETEC AUTOSCAN SCANNING ELECTRON MICROSCOPE. CARBON-CARBON SPECIMEN IS SHOWN LOADED IN STAGE.



FIGURE 39. TYPICAL SEM SPECIMEN. LOAD IS TRANSMITTED THROUGH THE EDGE NOTCHES IN THE TABS. THE CENTER HOLES ARE MERELY FOR ALIGNMENT PURPOSES.



FIGURE 40. SEM PHOTOGRAPH (SPECIMEN SEM-14) SHOWING CRACK WHICH INITIATED IN SHEAR (WHITE ARROW), PROPAGATED OPENING MODE, AND FINALLY TURNED  $90^\circ$  (TO SHEAR MODE AGAIN) AND RAN ALONG FIBER BUNDLE. 120X, 73 MPa (10.5 ksi). (LOADING DIRECTION IS OUTWARD IN HORIZONTAL DIRECTION).



FIGURE 41. SEM PHOTOGRAPH (SPECIMEN SEM-14)  
SHOWING CRACK RUNNING ACROSS TOP  
EDGE AND DOWN FRONT FACE OF  
SPECIMEN. 60X, 76 MPa (11.0 ksi).

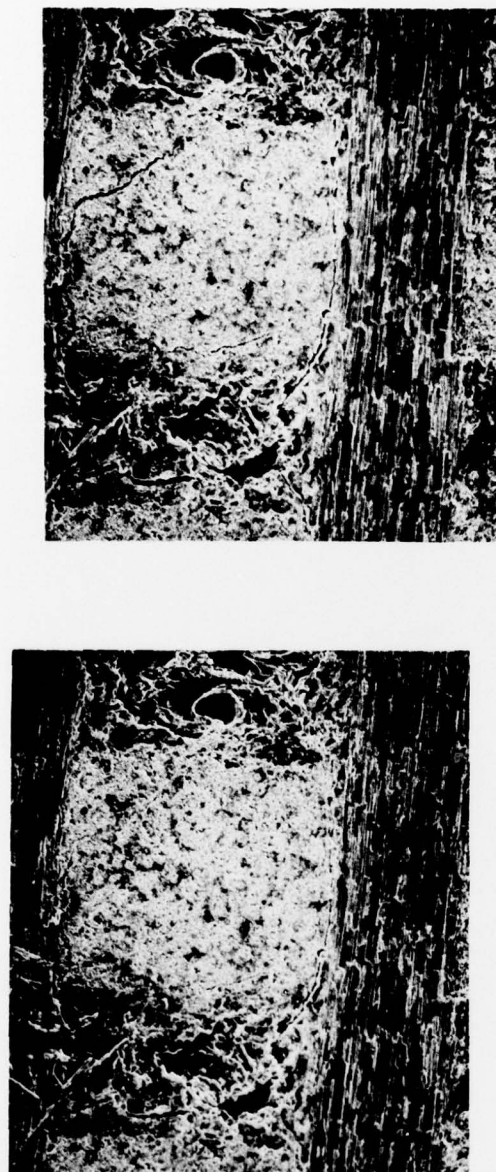


FIGURE 42. STEREO PAIR OF CRACK NETWORK (SPECIMEN SEM-20).  
40X, 15.9 MPa (2.30 ksi) FOR 42(a) and 66.2 MPa  
(9.60 ksi) FOR 42(b). HORIZONTAL DISPLACEMENT  
DIFFERENCES WILL APPEAR AS NORMAL DISPLACEMENTS  
WHEN STEREO PAIR IS CORRECTLY ALIGNED.

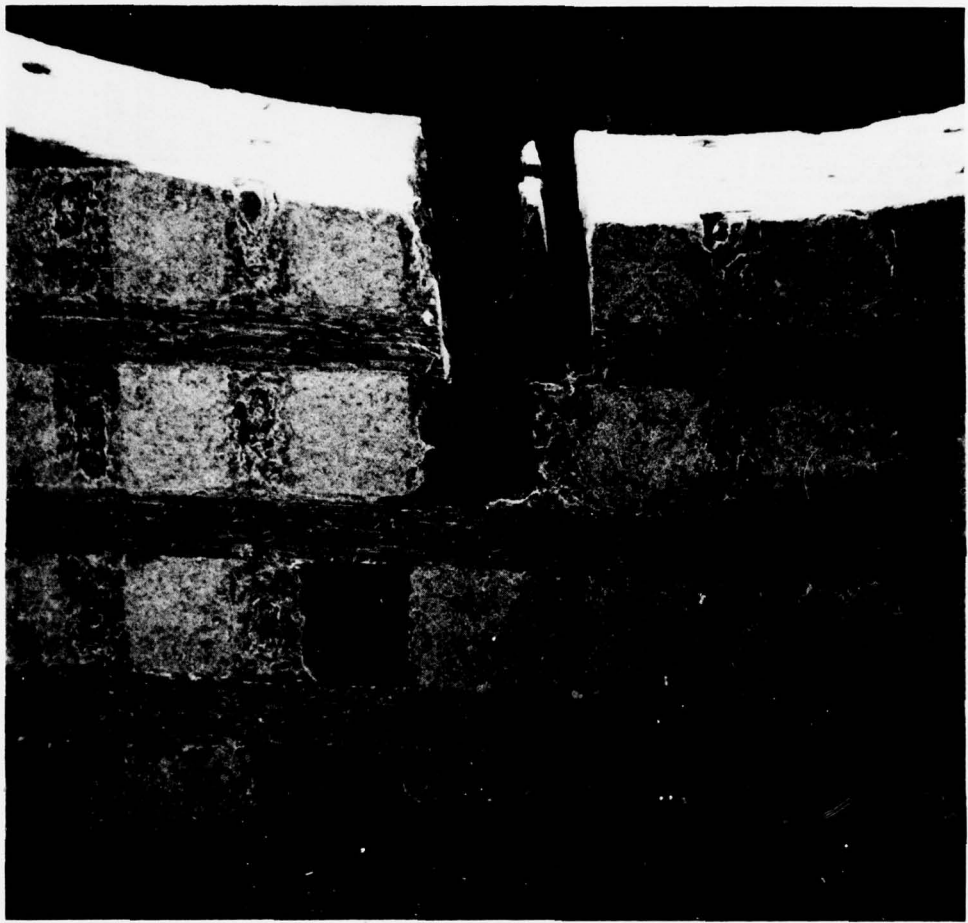


FIGURE 43. FAILED SEM SPECIMEN (SPECIMEN SEM-20), AT 17X.  
STARTER NOTCH (TOP OF SPECIMEN) PASSED THROUGH  
TOP FIBER BUNDLE.

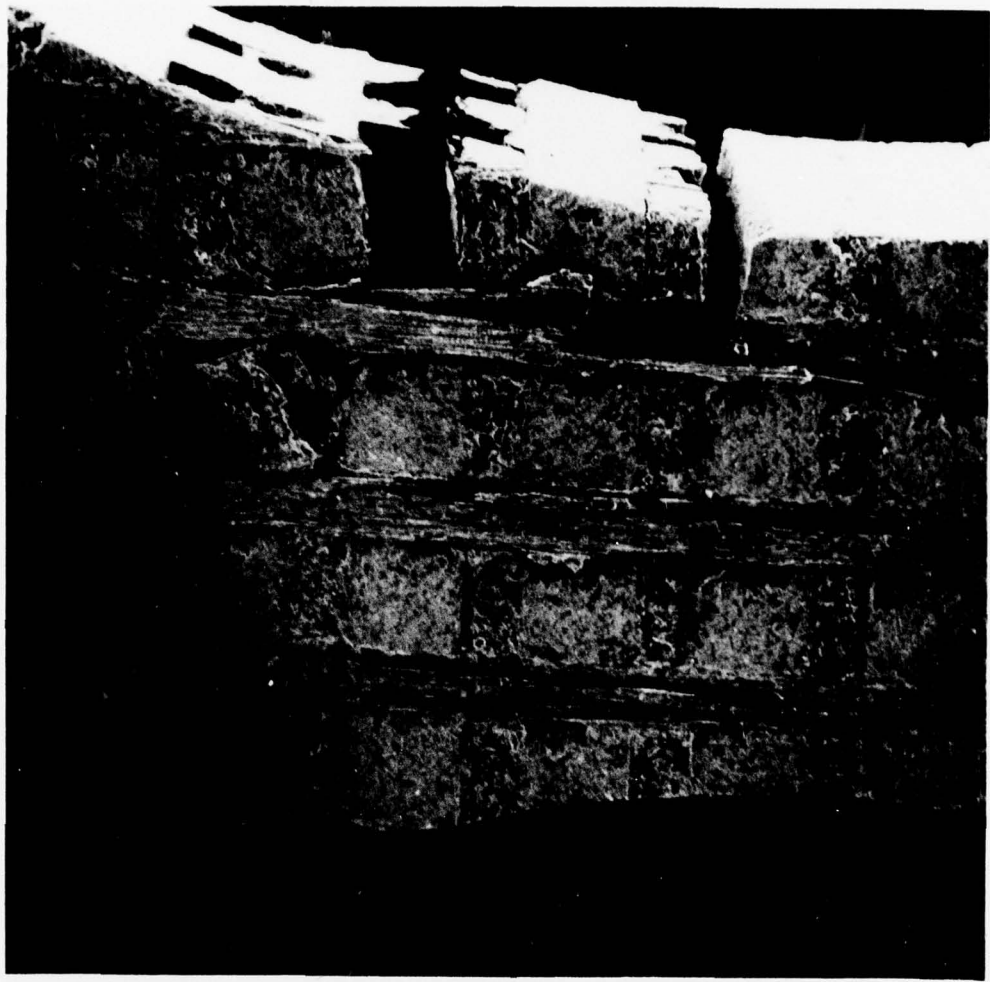


FIGURE 44. FAILED SEM SPECIMEN (SPECIMEN SEM-21), AT 17X.

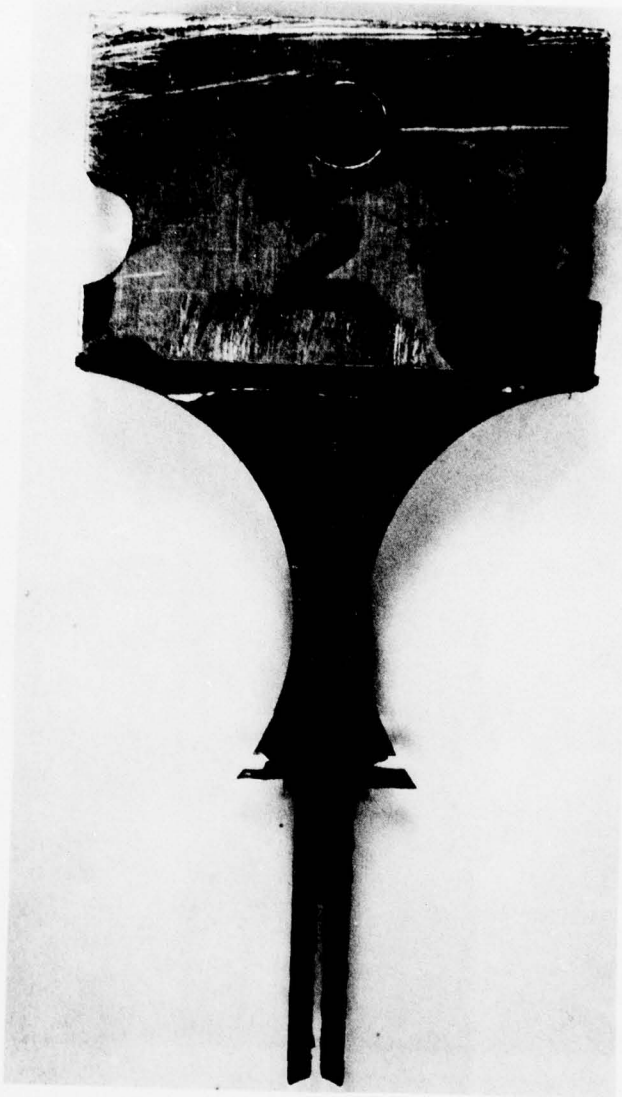


FIGURE 45. FAILED SEM SPECIMEN (SPECIMEN SEM-2,  
Z-DIRECTION).

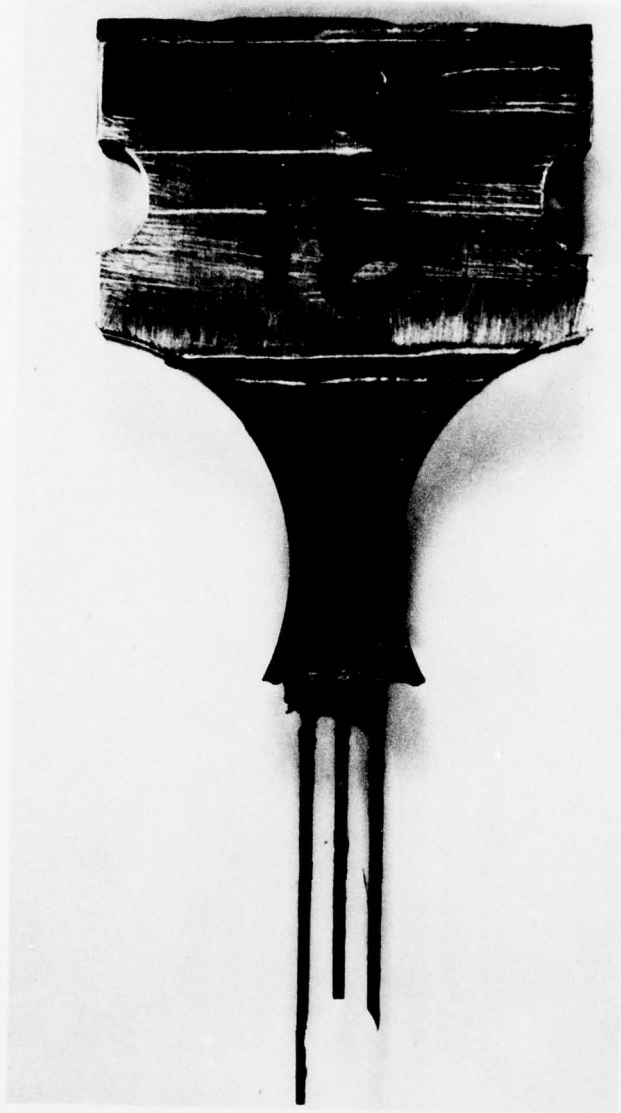


FIGURE 46. FAILED SEM SPECIMEN (SPECIMEN SEM-18,  
Y-DIRECTION).

## APPENDIX A

Page 1

DENSIFICATION ROUTING SHEET

Date Started: August 25, 1977 Date Finished: 11/27/77  
 FMI P/N: 2696 Finished Dimensions (in) Preform Density: .804 g/cc

Operation/Date	X	Y	Z	Weight (gms)	Volume	Density gms/cc	Approval, Remarks
Preform Density 8/25/77	4.290	4.289	8.571	2078	2585	.804	(S)
Radiographic Insp.							
Fixturing (Graphite Cage)		Frame No. 696		2956			(S)
1st Pitch Impreg. & Carb. 9/06/77	4.306	4.311	8.976	2871	2731	1.05	(S)
1st 5000 PSI PIC 9/09/77	4.344	4.334	8.924	3440	2753	1.25	(S)
1st Graphitization (2600°) 9/12/77	4.321	4.337	8.960	3335	2752	1.21	(S)
Skin Machined 9/13/77	4.179	4.184	8.333	3056	2391	1.28	(S)
2nd 5000 PSI PIC 9/16/77	4.210	4.207	8.378	3514	2432	1.44	(S)
2nd Graphitization (2600°) 9/19/77	4.201	4.185	8.375	3453	2413	1.43	(S)
3rd 5000 PSI PIC 9/22/77	4.196	4.207	8.362	3862	2420	1.60	(S)
3rd Graphitization (2600°) 9/26/77	4.208	4.200	8.370	3815	2424	1.57	(S)
4th 5000 PSI PIC 9/29/77	4.214	4.201	8.391	4117	2435	1.69	(S)
4th Graphitization (2600°) 10/03/77	4.215	4.204	8.386	4085	2435	1.68	(S)
5th 5000 PSI PIC 10/7/77	4.237	4.250	8.395	4302	2478	1.74	(S)
5th Graphitization (2600°) 10/10/77	4.233	4.222	8.380	4267	2455	1.74	(S)

## APPENDIX A (Cont'd)

Page 2

DENSIFICATION ROUTING SHEET (cont'd)

FMI P/N: 2696 (cont.)

Ray W. Carpenter  
In-Process Quality Control

Ray L. Carpenter  
In-Process Quality Control

## APPENDIX B

J. Phys. E: Sci. Instrum., Vol. 11, 1978. Printed in Great Britain

### A low-frequency cyclic-loading stage for the SEM

D L Davidson and A Nagy  
Southwest Research Institute, 8500 Culebra Road, San Antonio, Texas 78284, USA

Received 18 April 1977, in final form 23 August 1977

**Abstract** A cyclic-loading stage for the ETEC Corporation SEM is described. The stage uses servo-controlled electro-hydraulic loading with positive feedback. Specimens are loaded symmetric to the specimen centre line. Maximum load is 4893 N, with a maximum loading rate of 4 Hz. Resolution on the specimen is about 50.0 nm for static observation and 100.0 nm for dynamic (tv rate) observation in the secondary-electron mode. Observation of the specimen may also be made using backscattered electrons, and in the channelling mode (channelling patterns and channelling contrast). Maximum specimen motion during cyclic loading is 15  $\mu$ m.

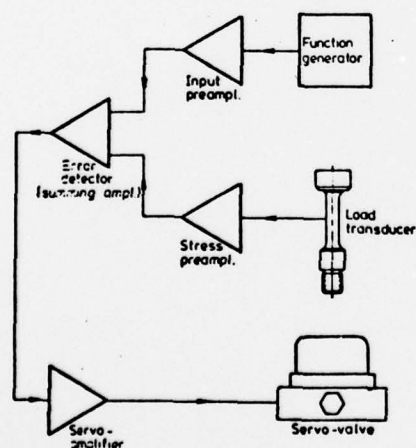


Figure 5 Diagram of control system.

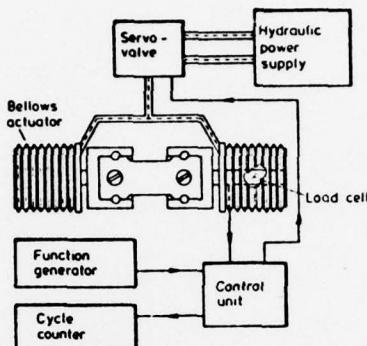


Figure 1 Diagram of loading and control system.

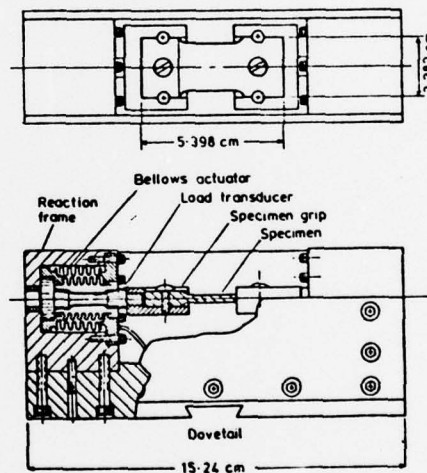


Figure 2 Loading system assembly with specimen.

DISTRIBUTION LIST

DOD

Office of the Secretary of Defense  
Director of Defense Research and  
Engineering  
    OAD/OS/Mr. B. Barse  
    OAD/ET/Mr. J. Persh  
    OAD/SW/Dr. R. Ruffine  
Washington, DC 20301

Plastics Technical Evaluation  
Center, Building 176  
ATTN: Mr. A. Anazione  
Department of Defense  
Picatinny Arsenal  
Dover, NJ 07801

Air Force Weapons Laboratory  
AFWL/

Lt. Col. D. Ericson  
Kirtland AFB, NM 87117

SAMSO/ABRES  
ATTN: Lt. Col. J. McCormack  
Worldway Postal Center  
P. O. Box 92960  
Los Angeles, CA 90009

Space and Missile Systems  
SAMSO/  
    MNNR/Capt. T. Brocato  
    MNPK/Capt. D. Bailey  
Norton AFB, CA 92409

AIR FORCE

Air Force Materials Laboratory  
AFML/

CC/Dr. F. Kelley  
MB/Mr. J. Kelble  
MBC/Dr. R. Craig  
MBC/Dr. W. Kessler  
MBC/Mr. D. Schmidt  
MBM/Dr. N. Pagano  
MX/Dr. M. Minges  
MXE/Lt. T. Curci  
MXE/Capt. E. Heinonen  
MXE/Mr. J. Latva  
MXE/Mr. G. Ormbrek  
MXE/Lt. G. Wendt  
LTN/Mr. H. Materne  
Wright-Patterson AFB, OH 45433

Air Force Office of Scientific Research  
AFOSR/NC/Dr. D. Ulrich  
    NC/Dr. D. Ball  
    NC/Dr. W. Walker/Dr. C. Hays  
    L/COL R. Haffner

Building 410  
Bolling AFB, DC 20332

Air Force Rocket Propulsion Laboratory  
AFRPL/

MK/Dr. C. Hawk  
MKC/Mr. L. Tepe  
MKCC/Mr. W. Payne  
CA/Mr. R. Weiss  
Edwards AFB, CA 93523

ARMY

Army Materials and Mechanics Research  
Center

ATTN: AMXMR-H/J. Dignam  
Watertown, MA 02172

NAVY

Assistant Secretary of the Navy (R&D)  
ATTN: Dr. S. Koslov  
Washington, DC 20301

Office of the Chief of Naval Operations  
ATTN: Mr. R. Blaise (OP-620E)  
Department of the Navy  
Washington, DC 20350

Director, Naval Research Laboratory  
ATTN: Dr. S. Freiman/Mr. P. Mast  
(Code 8434)  
Washington, DC 20375

Office of Naval Research  
ATTN: Dr. A. Diness (Code 471)  
800 North Quincy  
Arlington, VA 20305

Commander, Naval Sea Systems Command, HQ.  
ATTN: Mr. M. Kinna (SEA-0352)  
    Dr. J. Huth (SEA-03C)  
    Mr. G. Sorkin (SEA-035)  
Washington, DC 20302

<b>Commander</b>	<b><u>INDUSTRY (OTHERS)</u></b>
<b>Naval Surface Weapons Center</b>	
Mr. R. Edwards/Code WA-43	Acurex/Aerotherm
Mr. R. Feldhuhn/Code WA-43	ATTN: Mr. H. Tong
Dr. W. Lyons/Code WA-07	Mr. R. Manfred
Mr. C. Rowe/Code WR-31	Mr. J. Dodson
Mr. J. Vamos	Mr. J. Zimmer
Mr. J. Wagner/Code WA-43	485 Clyde Avenue
Mr. R. Wilson/Code WR-31	Mountain View, CA 94042
<b>White Oak</b>	
<b>Silver Spring, MD 20910</b>	
<b>Commander</b>	<b>Aerojet</b>
<b>Naval Weapons Center</b>	
Mr. J. Patton/Code 3161	ATTN: Mr. J. Cauzza
Mr. E. Jeter/Code 3162	Mr. H. Davis
<b>China Lake, CA 93555</b>	Mr. M. Clone
	Mr. R. Dona
<b>Director</b>	
<b>Strategic Systems Project Office (PM-1)</b>	
ATTN: Dr. J. Kincaid/SP-20	P. O. Box 13400
Dr. H. McMasters/SP-2723	Sacramento, CA 95813
Mr. S. Weinger/SP	
<b>Department of the Navy</b>	
<b>Washington, DC 20376</b>	
<b>Project Manager</b>	<b>Aeronutronic-Ford</b>
<b>Trident Systems Project (CNM-PM 2)</b>	
ATTN: Mr. J. Crone/HM-2-001	ATTN: Mr. J. Perry
<b>Department of the Navy</b>	
<b>Washington, DC 20360</b>	Ford Road
	Newport Beach, CA 92663
<b>NASA</b>	
<b>NASA, Marshall Space Flight Center</b>	
ATTN: Mr. B. Powers, EP 25	
<b>Huntsville, AL 35812</b>	
<b>DNA</b>	
<b>Director, Defense Nuclear Agency</b>	
ATTN: Mr. D. Kohler	<b>Aerospace Corporation</b>
Mr. J. Moulton	
<b>Washington, DC 20305</b>	ATTN: Dr. S. Batdorf
	Dr. H. Blaes
	Dr. S. Brelant
	Mr. J. Evangelides
	Dr. R. Hallse
	Mr. W. Herbig
	Dr. R. Meyer
	Mr. R. Mortensen
	Dr. L. Rubin
	P. O. Box 92957
	Los Angeles, CA 90009
<b>ERDA</b>	
<b>U.S. Energy Research Division</b>	
Administration	<b>Atlantic Research Corporation</b>
ATTN: Mr. A. Littman	
Nuclear Research and Application Div.	ATTN: Mr. W. Armour
Washington, DC 20331	Mr. J. Baetz
	Mr. J. Bird
	Mr. R. Brown
	5390 Cherokee Avenue
	Alexandria, VA 22314
	<b>Avco Corporation</b>
	ATTN: Mr. B. Benz
	Mr. G. Mullen
	Mr. A. Traverna
	Lowell Industrial Park
	Lowell, MA 01851
	<b>Avco Corporation</b>
	ATTN: Mr. P. Rolincik
	201 Lowell Street
	Wilmington, MA 01887

**Battelle Memorial Institute**  
ATTN: Mr. W. Chard  
505 King Avenue  
Columbus, OH 43201

**Boeing Company**  
ATTN: Mr. J. Bedwell  
P. O. Box 3996/MS 88-19  
Seattle, WA 98124

**California Research and Tech., Inc.**  
ATTN: Dr. K. Kreynenhagen  
6269 Dariel Avenue  
Woodland Hills, California 91364

**Carborundum Company**  
Graphite Products Division  
ATTN: Mr. W. Carlson  
2050 Cory Drive  
Sanborn, NY 14132

**Effects Technology, Inc.**  
ATTN: Mr. J. Green  
Mr. M. Graham  
5383 Hollister Avenue  
Santa Barbara, CA 93105

**Mr. D. Ehrentreis**  
Dave Ehrentreis Consulting Engr.  
5 Horizon Road  
Ft. Lee, NJ 07024

**Fiber Materials, Inc.**  
ATTN: Mr. L. McAllister  
Biddeford Industrial Park  
Biddeford, ME 04005

**General Electric Co., RESD**  
ATTN: Mr. P. Bolinger  
Dr. J. Gebhardt  
Mr. K. Hall  
Mr. D. Lowe  
Dr. E. Stover  
Mr. W. Reiley  
P. O. Box 7560 - Room 2023  
Philadelphia, PA 19406

**General Electric Co., RESD**  
ATTN: Mr. A. Levine  
3198 Chestnut Street  
Philadelphia, PA 19101

**Great Lakes Carbon Corporation**  
ATTN: Mr. W. Benn  
299 Park Avenue  
New York, NY 10017

**Great Lakes Research Corporation**  
ATTN: Mr. H. Gilliam  
P. O. Box 1031  
Elizabethton, IN 37643

**HAVEG**  
ATTN: Mr. R. Pegg  
Mr. R. Rodriguez  
12827 East Imperial Highway  
Santa Fe Springs, CA 90670

**Hercules Corporation**  
ATTN: Mr. P. Christensen  
Mr. K. Dickerson  
Mr. B. McKenzie  
P. O. Box 98  
Magna, UT 84044

**HITCO**  
ATTN: Mr. L. Dyson  
1600 West 135th Street  
Gardena, CA 90249

**Jet Propulsion Laboratory**  
ATTN: Mr. N. Kimmel  
Pasadena, CA 91103

**Kaiser**  
ATTN: Mr. M. Fischer  
Mr. W. Sidney  
880 Doolittle Drive  
San Leandro, CA 94577

**Lawrence Livermore Laboratories**  
ATTN: Mr. A. Maimoni (L-503)  
P. O. Box 808  
Livermore, CA 94550

**Lockheed Missiles and Space Company**  
ATTN: Mr. R. Greene  
Mr. G. Grunwald  
Mr. A. Johnson  
Mr. A. Mietz  
Dr. M. Steinberg  
P. O. Box 504  
Sunnyvale, CA 94088

**Los Alamos Scientific Laboratory**  
ATTN: Mr. R. Imprescia  
Dr. J. Taylor & C. Stein  
University of California  
P. O. Box 1663  
Los Alamos, NM 87545

**Materials Sciences Corporation**  
ATTN: Dr. S. Chatterjee  
Dr. J. Kibler  
Dr. B. Rosen  
**Blue Bell Office Campus**  
**Merion Towle Building**  
**Blue Bell, PA 19422**

**McDonnell Douglas Astronautics Co.**  
ATTN: Mr. L. Greszczuk  
Mr. J. Jortner  
Mr. B. Leonard  
Dr. J. Peck  
Mr. A. Penton  
Mr. R. Seibold  
**5301 Bolsa Avenue**  
**Huntington Beach, CA 92647**

**McDonnell Douglas Research Labs.**  
ATTN: H. Holman  
P. O. Box 516  
**St. Louis, MO 63166**

**NETCO**  
ATTN: Mr. W. Pfeifer  
Ms. P. Sullivan  
Mr. R. Young  
**110 Pine Avenue, Suite 906**  
**Long Beach, CA 90802**

**Prototype Development Associates, Inc.**  
ATTN: Mr. Alexander  
Dr. G. Crose  
Dr. J. McDonald  
Mr. G. Schutzler  
**1740 Garry Avenue, Suite 201**  
**Santa Ana, CA 92705**

**Sandia Laboratories**  
ATTN: Mr. D. Northrup  
P. O. Box 5800  
**Albuquerque, New Mexico 87115**

**Science Applications, Inc.**  
ATTN: Mr. F. Clayton  
Mr. D. Eitman  
Mr. K. Kratsch  
Dr. W. Loomis  
Mr. J. Pope  
Dr. P. Randles  
**201 West Dyer Road, Unit C**  
**Santa Ana, CA 92707**

**Southern Research Institute**  
ATTN: Mr. C. Canada  
Mr. H. Littleton  
Mr. H. Starrett  
Mr. C. Pears  
**2000 Ninth Avenue, South**  
**Birmingham, AL 35205**

**Southwest Research Institute**  
ATTN: Dr. Philip H. Francis  
Dr. J. Lankford  
P. O. Drawer 28510  
**San Antonio, TX 78284**

**Stackpole Fibers Company, Inc.**  
ATTN: Mr. G. Flemming  
Foundry Industrial Park  
**Lowell, MA 01852**

**Super-Temp Company**  
ATTN: Mr. D. Bauer  
111205 Norwalk Boulevard  
**Santa Fe Springs, CA 90670**

**Systems, Science and Software**  
ATTN: Mr. C. Emde  
Dr. G. Gurtman  
P. O. Box 1620  
**La Jolla, CA 92037**

**Thiokol**  
ATTN: Mr. G. Broman  
Dr. S. Kulkarni  
Mr. A. Canfield  
Mr. R. Laramee  
**Brigham City, UT 84302**

**TRW Systems Defense Space Systems**  
ATTN: Dr. W. Kotlensky  
Building R-1-Room 2012  
One Space Park  
**Redondo Beach, CA 90278**

**Union Carbide Corporation**  
Nuclear Division (Y-12 Plant)  
ATTN: Mr. A. Taylor  
Dr. G. Weber  
P. O. Box Y  
**Oak Ridge, TN 37839**

**Union Carbide Corporation**  
Carbon Products Division  
ATTN: Mr. J. Bowman  
Dr. J. Criscione  
P. O. Box 6116  
**Cleveland, OH 44101**

**United Technologies**  
Chemical Systems Division  
ATTN: Mr. R. Ellis  
Mr. P. O'Driscoll/Mr. S. Slosarik  
P. O. Box 358  
**Sunnyvale, CA 94088**

UNIVERSITIES

Department of Physics and Astronomy  
Ball State University  
ATTN: Mr. S. Mrozowski  
Muncie, IN 47306

Franklin Institute Research Labs.  
Physics of Materials Laboratory  
Material and Physical Sciences Dept.  
ATTN: Mr. J. Meakin, Manager  
Benjamin Franklin Parkway  
Philadelphia, PA 19103

Applied Physics Laboratory  
The Johns Hopkins University  
ATTN: Mr. W. Caywood  
Johns Hopkins Road  
Laurel, MD 20810

Department of Materials Science and  
Engineering  
Massachusetts Institute of Technology  
ATTN: Dr. D. Uhlmann  
Boston, MA 02139

Massachusetts Institute of Technology  
ATTN: Mr. J. May  
Dr. J. W. Mar  
Boston, MA 02139

Aeronautical Research Associates of  
Princeton  
ATTN: Dr. T. McDonough  
Washington Road  
Princeton, NJ 08540

Materials Science Department  
Pennsylvania State University  
ATTN: Dr. P. Walker  
State College, PA 16801

Department of Materials Engineering  
Rensselaer Polytechnic Institute  
ATTN: Dr. J. Diefendorf  
Troy, NY 12181

Southern Methodist University  
Civil and Mechanical Engineering  
Department  
ATTN: Dr. R. M. Jones  
Dallas, TX 75275

University of California, Los Angeles  
School of Engineering and Applied Science  
ATTN: Dr. G. Sines  
Los Angeles, CA 90024

Department of Mining, Metallurgical  
and Ceramic Engineering  
University of Washington  
ATTN: Mr. D. Fischbach  
Mr. D. Uptegrove  
Seattle, WA 98195

University of Wyoming  
Department of Mechanical Engineering  
ATTN: Dr. D. Adams  
Laramie, WY 82071

University of Southern California  
ATTN: Mr. T. Yen  
Los Angeles, CA 90007